TEL AVIV UNIVERSITY

THE IBY AND ALDAR FLEISCHMAN FACULTY OF ENGINEERING

CYCLOTRON-RESONANCE MASER ARRAYS AND THEIR ELEMENTS

Thesis submitted for the degree of

"Doctor of Philosophy"

By

Amit Kesar

Submitted to the Senate of Tel Aviv University

August 2002

TEL AVIV UNIVERSITY

THE IBY AND ALDAR FLEISCHMAN FACULTY OF ENGINEERING

CYCLOTRON-RESONANCE MASER ARRAYS AND THEIR ELEMENTS

Thesis submitted for the degree of

"Doctor of Philosophy"

By

Amit Kesar

This research work was carried out under the supervision of

Prof. Eli Jerby

Submitted to the Senate of Tel Aviv University

August 2002

Acknowledgments

Since our first meeting, I kept feeling the enthusiasm, creative ideas, encouragement and support of my research supervisor, Prof. Eli Jerby. I deeply thank him for his care, concern, and guidance during this thesis work.

A deep thank to Moshe Einat for helping me in many parts of this thesis. His experience and many hours of discussions provided me with valuable advises. I enjoyed working with him.

I thank my colleagues Alon Aharony, Oleg Aktushev, David Armoni, David Blank, Gregory Breitmeier, Vladimir Dikhtiar, Rami Drori, Assaf Hazzan, Michael Korol, Li Lei and Avi Shahadi for their helpful contribution.

I wish to thank my parents - Sara and Shlomo, my sisters - Shiffi and Raya, and my brothers - Shlomi and Itai, for their encouragement and help during all these years.

Most of all, my sincere gratitude to my wife, Sharon, for her advises, encouragement, and support.

Abstract

Cyclotron-resonance masers (CRMs) and gyrotrons are sources for high-power microwaves. The high output power is achieved by the interaction of the electromagnetic wave with a high-voltage high-current electron beam. However, several technological difficulties are associated with high-voltage and current operation. The CRM-array concept was proposed by Jerby in order to overcome these difficulties, and to enable new features such as the active antenna. This thesis presents a theoretical and experimental study of multiple electron-beam CRM arrays. In such schemes, the electromagnetic wave interacts with many low-voltage low-current electron beams instead of the single high-power beam in the conventional device. Characteristics and unique features of the CRM-array concept are studied theoretically and experimentally for uncoupled and coupled CRM-arrays.

A theoretical study of lobe steering by an uncoupled CRM-array is presented. The array consists of single-beam CRM-elements, all sharing the

same axial magnetic field. The CRMs radiate directly from their apertures to form an active array antenna. The radiation is integrated in the far-field and is proportional to the entire CRM-array output-power. The gain and phase-shift of the CRM-element are synthesized by a linear model with respect to the electron-gun voltage and current. Phased-array radiation patterns are demonstrated by choosing operating points of constant gain and equal phase-shift between adjacent CRM-elements.

The characteristics of the CRM-array are determined by its elements. Three schemes of CRM-elements are studied in this thesis. All of them are aimed to be compact-devices that operate at low electron-beam voltage. The first scheme demonstrates phase and gain measurements in a CRM-amplifier. Following Chu *et al.* [Phys. Rev. Lett. **74**, (1995)], the CRM-amplifier comprises of a distributed-loss waveguide to enable high gain without oscillations. In this scheme the gain and phase-shift are measured with respect to the axial magnetic field and the e-beam current. The device was operated at a low e-beam voltage of 18 kV. An output power of 0.63 kW corresponds to a maximum gain of 26 dB and a non-saturated efficiency of 12% was measured at 7.3 GHz. A full 360° phase-shift range at a constant gain of 23 dB was obtained by tuning simultaneously the axial magnetic field and e-beam current. The obtained results were in a good agreement with theoretical non-linear calculations. Such device can be integrated as an element in a low-voltage

CRM-array.

The second scheme consists of a controlled feedback oscillator. The output of the distributed-loss CRM-amplifier was coupled back into its input port through a controlled 3-state phase-shifter. Oscillations were obtained when the total gain of the CRM plus feedback was above unity, thus pulse modulations are enabled by modulating the phase shifter 'on' and 'off'. Frequency modulations were obtained by varying the feedback phase-shift. Such scheme can be applied for CRM-array oscillators, where the controlled feedback from a single element can drive in-phase the entire array.

The third scheme presents a novel concept of a CRM with a ferrite loading incorporated in its waveguide. The CRM interaction occurs between the rotating electron-beam and the electromagnetic wave propagating along a longitudinally magnetized ferrite medium. The ferrite unisotropic permeability resembles the CRM susceptibility in many respects, and in particular in their similar response to the axial magnetic field (the ferrite susceptibility can be regarded as a passive analogue of the active CRM interaction). The ferrite loading enables a new mechanism of spectral tunability for CRMs. The ferrite loading can serve as a useful ingredient for high-power CRM devices. A linear model of the combined ferrite-guided CRM interaction is presented. Numerical examples demonstrate a wide tunability range, from 8.3 to 9.5 GHz, with a very low operating voltage of 7.5 kV. These properties

could be used in a new scheme of a tunable CRM-array antenna.

The coupled CRM-array subject is studied in a four electron-beam CRM-oscillator scheme. The cavity consists of a periodic waveguide in which consequent vertical and horizontal metallic posts divide its cross section to four quarters. Four electron beams (17 kV, 0.7 A each), located symmetrically around the quarters, travel in a cyclic motion along the waveguide under the axial magnetic force of a common external solenoid. When the electron-beams were operated simultaneously, an output power of 710 W was measured at frequency of 3.9 GHz, within the pass-band of the periodic waveguide. When each electron-beam was operated alone, the output power was 250 W or less. A possible synergism effect is shown for a combined operation of three electron-beams. A reduction in the output power for a combined operation with one of the beams is explained due to a mechanical deviation. In a second scheme, in which the an additional reflector was added at the beginning of the interaction region, the output power was summed only from the operation of each two diagonal channels. Adjacent channel operation resulted in a power cancellation.

The CRM-array studies presented in this thesis might be useful for high-power applications in which low-voltage operation along with a compact scheme is essential. Such applications might include radars, material processing, and communications.

List of publications

Papers

1. A. Kesar and E. Jerby, "Radiation beam steering by cyclotron-resonance maser array," *Physical Review E*, vol. 59, pp. 2464–2466, 1999.

2. E. Jerby, A. Kesar, M. Korol, L. Lei, and V. Dikhtiar, "Cyclotron-resonance maser arrays," *IEEE Transactions on Plasma Science*, vol. 27, pp. 445–455, 1999.

3. G. S. Nusinovich, O. V. Sinitsyn, and A. Kesar, "Linear theory of gyro-traveling-wave-tubes with distributed losses," *Physincs of Plasmas*, vol. 8, pp. 3427–3433, 2001.

4. A. Kesar and E. Jerby, "Phase and gain measurements in a distributed-loss cyclotron-resonance maser amplifier," *Physical Review E*, vol. 65, pp. 036503/1–6, 2002.

5. E. Jerby, A. Kesar, A. Aharony, and G. Breitmeier, "Ferrite-guided cyclotron-resonance maser," *Physical Review E*, vol. 65, pp. 066502/1–8, 2002.

6. M. Einat, E. Jerby, and A. Kesar, "Anomalous free electron laser interaction," *Nuclear Instruments and Methods in Physics Research A*, vol. 483, pp. 482–487, 2002.

7. M. Mashevich, D. Folkman, A. Kesar, A. Barbul, R. Korenstein, E. Jerby, and L. Avivi, "Exposure of human peripheral blood lymphocytes to electromagnetic fields associated with cellular phones leads to chromosomal instability." Submitted to Bioelectromagnetics, 2002.

Conference Oral Presentations

1. A. Kesar and E. Jerby, "Power-beam steering by a CRM array," in *Int'l Research Workshop on CRMs and Gyrotrons*, Kibbutz Ma'ale Hachamisha, Israel, May 18-21, 1998.

2. A. Kesar and E. Jerby, "Spatial steering of CRM array antenna by magnetic fields," in *The Fourth Israeli Conference on Plasma Science and its Applications*, Technion - Israel Institute of Technology, Haifa, Israel, February 15, 2001.

Conference Posters

1. A. Kesar, D. Blank, and E. Jerby, "Cyclotron-resonance maser array antenna," in *IEEE Int'l Conference on Plasma Science*, Banff, Alberta, Canada, May 26-30, 2002.

2. A. Kesar, D. Blank, and E. Jerby, "Amplitude locking in a gyro-TWT amplifier with a delayed feedback," in *IEEE Int'l Conference on Plasma Science*, Banff, Alberta, Canada, May 26-30, 2002.

Contents

Chapter 1

Introduction

High-power microwave generation and amplification are a subject of great importance in modern science and technology [1, 2]. Cyclotron-resonance masers (CRMs) in general and gyrotrons in particular [3, 4], are used in the millimeter and sub-millimeter regimes. Candidate application examples are in material processing [5], nuclear reactors [6], accelerators [7], and radars [8]. All these high-power gyrotrons and CRMs use a single electron-beam which interacts with an electromagnetic (em) wave inside a waveguide.

The principle of cyclotron-resonance interaction is as follows. The electron beam travels along the waveguide in a cyclic motion, caused by an axial magnetic field. A synchronism condition is achieved when the wave frequency equals the cyclotron frequency, or its nth harmonic frequency, plus a Doppler

shift,

$$\hat{\vartheta} = (\omega - n\omega_c - k_z V_z)\tau_0 \approx 0, \tag{1.1}$$

where $\hat{\vartheta}$ is the normalized tuning parameter, and the *em* angular frequency and its wavenumber are ω and k_z, respectively. The cyclotron frequency is

$$\omega_c = \frac{eB_z}{\gamma m_0}, \tag{1.2}$$

where the electron charge and rest-mass are e and m_0, respectively, γ is the relativistic factor, B_z is the axial magnetic field, V_z is the electron axial-velocity, and $\tau_0 = L/V_z$ is the electron time of flight along the interaction region, L.

The development in the research revealed that CRMs can be useful for a variety of applications. A comprehensive review on the state-of-the-art gyrotrons is presented by Thumm [9]. Some of the significant achievements and their applications include:

(a) Gyrotron oscillators for CW powers of 1–40 kW and frequencies of 23–326 GHz. Gyro-TWT amplifiers for 93 kW, 70 dB, 33.6 GHz, 8.6% bandwidth [10], for 28 kW, 31 dB, 93.7 GHz, 2% bandwidth, and for 3 MW, 33 dB, 37 GHz, 20% bandwidth. These gyrotrons are useful for technological applications like communications and power industry.

(b) Gyrotron oscillators for CW powers of 140–340 kW and frequencies of 28-70 GHz, useful for electron-cyclotron resonance heating (ECRH).

(c) Relativistic gyrotron oscillators for 30 MW, 79–107 GHz, for 1 GW, 8.35–13 GHz, and for 1.8 GW, 3.1 GHz.

(d) Second-harmonic gyrotrons for the mm- and sub-millimeter-waves for frequencies of 157–576 GHz and powers of several kilowatts, and a third-harmonic gyrotron for 889 GHz [11], that can be useful for plasma scattering measurements and electron-spin resonance experiments.

The efficiency of most of the gyrotrons is in the range of 30–68% with a single-step depressed collector. The major goal is to develop efficient gyrotrons capable of producing CW powers of several megawatts at frequencies of 28–170 GHz for ECRH applications. A current solution is to use several separate $\sim$ 1 MW gyrotrons and to combine their power by quasi-optical mirrors [12, 13]. Another major goal is to develop repetitive pulse sources to hundreds of megawatts at frequencies of 17-35 GHz as accelerator drivers and also for applications like super-range high-resolution radar and atmospheric sensing.

All of the gyrotrons listed above use a single high-power electron beam. The output power in CRM devices can be increased by increasing the beam energy and current [14]. Some of the difficulties and disadvantages related to high-power devices are as follows. The disadvantage in high-energy operation is related mostly to the overhead of the device: large electron-gun and collec-

tor sections [15], complexity in power supplies, insulators and safety shields. The disadvantage in a high-current electron-beam is related to the space-charge effect which decreases the beam quality, hence thereby decreasing the device efficiency [16]. Another difficulty is related to the output window, in which part of the output power is dissipated, and therefore the window should be cooled [17].

The multi-beam CRM-array concept was proposed by Jerby *et al.* [18, 19]. This concept suggests to increase the output power by increasing the CRM dimensionality, i.e. increasing the number of interaction channels and electron-beams in the device, rather than increasing the single-beam energy and current. In this way, many low-energy low-current electron-beams interact simultaneously inside large 2D (two dimensional) or 3D CRM-arrays and amplify the *em* wave. The output power can be distributed through a large output window that covers the entire array aperture. A conceptual scheme of a multi-beam CRM-array is shown in Figure 1.1. In this figure an array of electron beams is generated by a cathode array. The beams interact with the *em* wave inside a 3D lattice-like waveguide. An axial magnetic field supports the cyclotron synchronism between the electron beams and the wave. The beams are collected by a collector array, while the *em* wave is radiated directly from the CRM-array aperture.

The multi-beam CRM-arrays can be classified in two groups according to

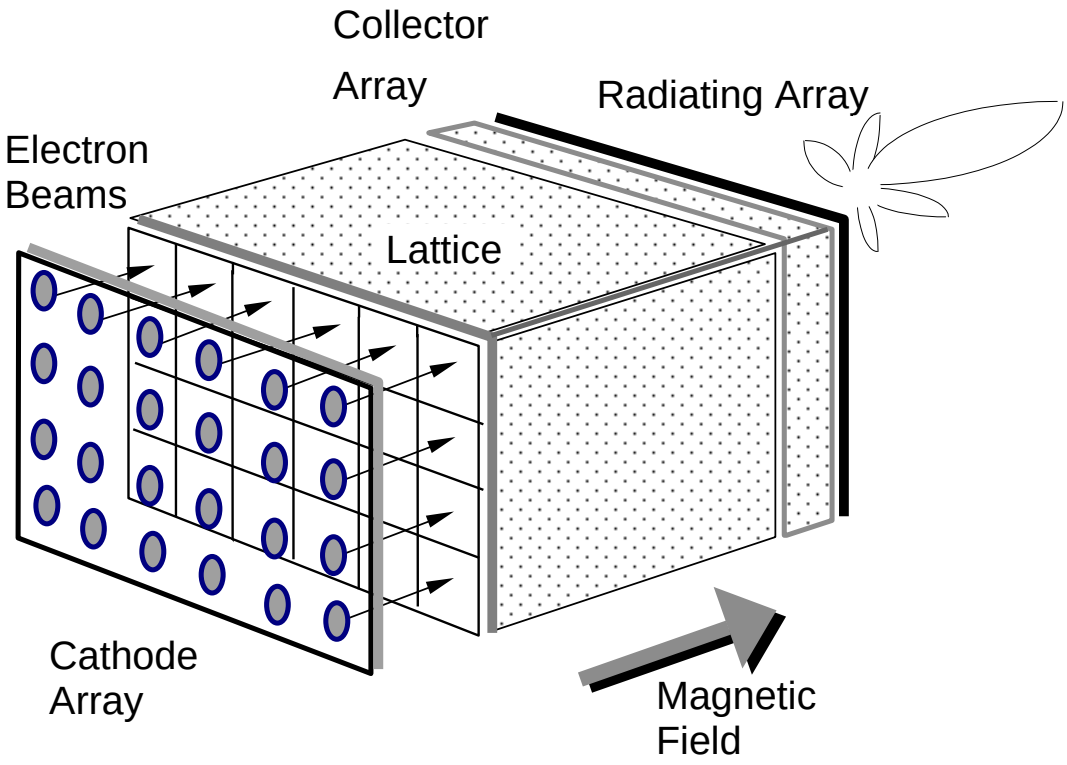

Figure 1.1: Conceptual scheme of a multi-beam CRM-array [19]

the coupling between the electron-beams. The first group is the uncoupled CRM-array, which consists of an array of uncoupled single CRM-elements. The output power from all the CRM-elements can be accumulated in the far field. Hence, the uncoupled CRM-array can operate as an active CRM-array antenna. The only coupling between the elements can be physical (for example, they all share the same solenoid that produces the axial-magnetic field), or due to external reflections between the elements. The second group is the coupled CRM-array, which consists of an array of electron-beams inside a single cavity or waveguide. In this case the beams are coupled by one *em*

wave. The studies described in this thesis demonstrate features of multi-beam CRM-arrays: the uncoupled CRM-array, including three related studies of the possible CRM-elements, and a study of the coupled CRM-array.

Chapter 2 in this thesis describes a new concept of radiation beam steering by a CRM-array [20]. In this chapter a linear theory is used to calculate the gain and phase-shift of the uncoupled CRM-element, with respect to its beam voltage and current. A phased-array radiation pattern is calculated by controlling simultaneously these beam parameters for the entire array. The CRM-array radiates directly from its element-apertures, and thus operates as an active antenna array. The radiation integrated in the far-field is proportional to the number of operating CRM-elements and the power of these elements. The CRM-array antenna could be used in various applications, including radars, power beaming, plasma heating, and material processing. Chapters 3–5 demonstrate three low-voltage and compact single-beam studies that can be applied for the CRM-element.

The distributed-loss CRM amplifier experiment is described in Chapter 3 [21]. It demonstrates the ability to control the phase-shift in a 360° range while keeping a constant power-gain by slight tuning of the solenoid field and the e-beam current. This experiment, carried out at low electron-beam voltage and current (< 18 kV, < 0.4 A), has shown a maximum power gain of 26 dB (0.63 kW, 12% efficiency). The high-gain was enabled by using

a waveguide incorporating distributed losses. It extends the results shown by K. R. Chu *et al.* [10] to these operating parameters. The results of this experiment are also important for phase-stability related-studies such as for radar applications and for driving particle accelerators.

Chapter 4 describes amplitude and frequency modulations by a feedback-controlled oscillator [22]. In this experiment a coupling of the CRM-amplifier output was connected by a feedback into its input port. The feedback included a 3-state electronically-controlled phase-shifter (0 and 180° phase-shift states, or an 'off' state). Such scheme could be applied for controlling CRM-array oscillators to operate in-phase, by coupling a single-element output through a controlled feedback into the inputs of the array elements.

Chapter 5 describes a theoretical study of a ferrite-guided CRM. The waveguide is partially filled by a ferrite material. The ferrite loading slows the wave and enables an axial (Weible) bunching mechanism. Unlike periodic or dielectric loads for slow-wave CRM's, the ferrite permeability is a resonant effect governed by the same axial (static) magnetic field incorporated in the CRM device itself. The linear model presented in this chapter shows that the ferrite loading may enable a new tuanbility feature of the CRM interaction since the waveguide spectral response is tuned simultaneously with the CRM interaction by the static magnetic field. Such tuning at low-voltage conditions could not be achieved in regular (hollow) waveguides. This scheme may

enable tunable CRM-arrays.

Chapter 6 describes a multi-beam CRM experimental study [23]. Four electron-beams interact simultaneously with the *em* wave in a periodic waveguide. This study shows also the ability to operate the multi-beam CRM with a wide cross-sectioned waveguide and avoid exciting parasitic modes. The periodic loading also enables the operation with low-energy electron-beams.

The results in this thesis could provide a significant step towards the design of large CRM-arrays that will produce high-power microwaves. These arrays may alleviate the technological difficulties of one-dimensional devices that result from the high-voltage and high-current operation and from the high power density that is transferred through the output window. The proposed direct radiation with lobe steering abilities can lead to the development of high-power high-resolution radars and to improvements in industrial applications such as material processing and communication systems. The gain and phase study can be useful also for accelerator-driving applications.

Chapter 2

Radiation Beam Steering by CRM Array

The CRM-array antenna consists of many uncoupled CRM-elements. In each CRM-element a single low-energy low-current electron beam is propagating along its waveguide. The total high-power radiation beam is combined in space [18].

A linear model of the CRM-array interaction is presented in Ref. [24], and first experiments are described in Ref. [25]. A stagger-tuned multibeam gyroklystron was proposed and analyzed as a wideband amplifier [26]. This chapter presents an advanced feature of the CRM-array, as an active phased-array antenna with electronic steering abilities.

Power beaming, as a concept of launching directed high-power energy to

space, is attractive in areas like communication, radar systems and plasma heating for fusion [27]. This concept is also explored for military purposes like directed energy weapons [28] and for energy transfer to distant targets [29, 30].

Phased-array antennas are usually known as passive devices [31]. They are fed by external microwave sources. The radiation is divided to the radiating elements, usually through ferrite phase-shifters. The radiation steering is accomplished by varying the phase shifts between the elements. Active phased-array antennas consist, in general, of many power-amplifier elements, each of them is tuned to a proper phase in order to build the required far-field radiation lobe, as in Ref. [32]. Similar devices were developed on the basis of traveling-wave-tube multi-beam-arrays (MBAs), and of solid-state amplifier arrays [33]. Angular-steering in free-electron laser (FEL) arrays was proposed and studied as well [34].

The concept of the CRM-array antenna presented in this chapter is published in Ref. [20]. All of the CRM-elements are sharing the same axial magnetic field [35]. A conceptual scheme of the CRM-array antenna is shown in Fig. 2.1. The input *em* wave is injected equally to all the CRM elements in the array. The angular steering of the far-field radiation is accomplished by varying the amplitude and phase of each CRM element. This is done by controlling the accelerating voltage and the electron current of each electron

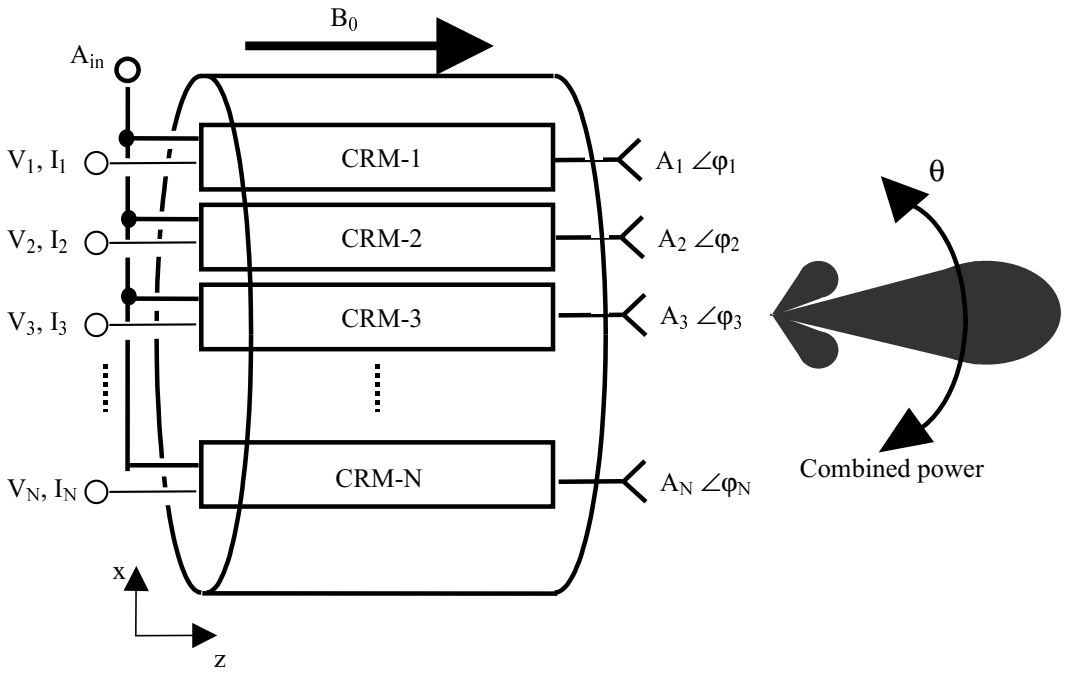

Figure 2.1: A conceptual scheme of the CRM-array antenna.

2.1 Linear model

A simplified CRM-array antenna model is derived in this section in order to demonstrate the concept. The gain and phase-variation at the CRM output depend on the physical operating parameters of each element; the em wave frequency (ω), the axial magnetic field (B_{0z}), the electron accelerating voltage (V_{eb}) and current (I_{eb}), and the waveguide structure. In this preliminary study, we assume that the CRM-elements in the array are not coupled by

Table 2.1: CRM-array parameters.

Axial magnetic field B_{0z}	2.57 kG
Frequency f	8.2 GHz
Electron beam current I_{eb}	0.5–1.5 A
Electron beam voltage V_{eb}	8–25 kV
Pitch ratio $V_\perp/V_z$	1
Interaction length L	1 m
Number of elements N	10, 25
Phase difference between neighbor elements $\Delta\varphi$	0°, 30°, 60°
Maximum steering angle θ	0°, 17°, 35°

the waveguide structure.

A linear analysis of the CRM interaction results in a known Pierce-type gain-dispersion relation [36], applicable for the nth element in the uncoupled array as

$$\tilde{A}_n(\hat{s}) = \frac{(\hat{s}-\hat{\theta}_n)^2}{\hat{s}(\hat{s}-\hat{\theta}_n)^2 - Q_n(\hat{s})} A_0, \tag{2.1}$$

where A_0 and $\tilde{A}_n(\hat{s})$ are the input and output fields, respectively, of the nth CRM element, and $\hat{s}$ denotes the normalized Laplace transform variable. The normalized tuning parameter is $\theta_n = (\omega - \omega_{c,n} - \beta\bar{V}_{0z,n})\tau_{0,n}$, where

$\tau_{0,n} = L/\bar{V}_{0z,n}$ is the electron time of flight along the interaction region, L. The em wavenumber $\beta(\omega)$ is determined by the waveguide dispersion relation. The cyclotron frequency is $\omega_{c,n} = eB_{0z}/\gamma_n m_0$. The gain parameter Q_n depends on the nth electron beam current and energy, and on other parameters as described in Ref. [36].

Assuming that each CRM-element radiates from a separate rectangular aperture (TE_{10} mode), and is not coupled to the other elements, the broadside far-field radiation of the nth element is the aperture Fourier transform [31], $f_x^{(n)}(k_x) = \int_x E_x^{(n)} e^{jk_x x} dx$, where k_x is the wave wavenumber component in the x direction, and $E_x^{(n)}$ is the electric field profile on the aperture. For the entire CRM-array antenna, the total far-field radiation is the sum

$$F_x^{(n)}(k_x) = \sum_{n=1}^{N} f_x^{(n)}(k_x) A_n e^{j(nk_x d - \varphi_n)}, \tag{2.2}$$

where A_n and φ_n are the amplitude and phase, respectively, of each CRM-element output. The elements are separated by a distance d in the x direction. In spherical coordinates (r, θ), where $k_x = k\sin(\theta)$, the far-field is [31]

$$E_\theta(\theta) = jk\frac{e^{-jkr}}{2\pi r} F_x \,. \tag{2.3}$$

The power density is given by the Poynting vector $|S| = |E \times H| = |E_\theta|^2/2Z_0$. The numerical solution dictates how to control $V_{eb}^{(n)}$ and $I_{eb}^{(n)}$ in order to synthesize the desired amplitude and phase difference between the CRM elements.

2.2 Numerical examples for CRM steering

The gain-dispersion relation (2.1) is solved numerically for the parameters shown in Table 2.1. Fig. 2.2 shows the CRM output in a contour plot of gain and phase vs. electron-beam current and voltage. This graph is useful for the synthesis of the CRM-element operating conditions according to the desired amplitude and phase. It can be seen that a full 360° phase range is achieved between $-110°$ and 250° for the 150 gain contour. To obtain this, the electron-beam current should be varied between $\sim$ 0.7 and 1-A with a corresponding voltage between $\sim$ 10 and 24-kV. This 150 gain contour is less than 2 dB than the maximum gain available within this window range.

An active phased-array radiation pattern is obtained by choosing the operating conditions of the CRM-elements on a constant gain contour and an equal phase-shift between adjacent elements. These complex CRM-element output signals, $A_n \angle \varphi_n$, synthesized by Fig. 2.1, are used in Eq. (2.2) to calculate the far-field radiation pattern. Figs. 2.3(a) and 2.3(b) show examples of radiation patterns in different steering conditions for arrays of 10 and 25 CRM elements, respectively. A steering angle of 35° is obtained for a phase shift of 60° between each two adjacent CRM elements in the array. As expected, the 25-element array provides higher gain and directivity than the 10-element array.

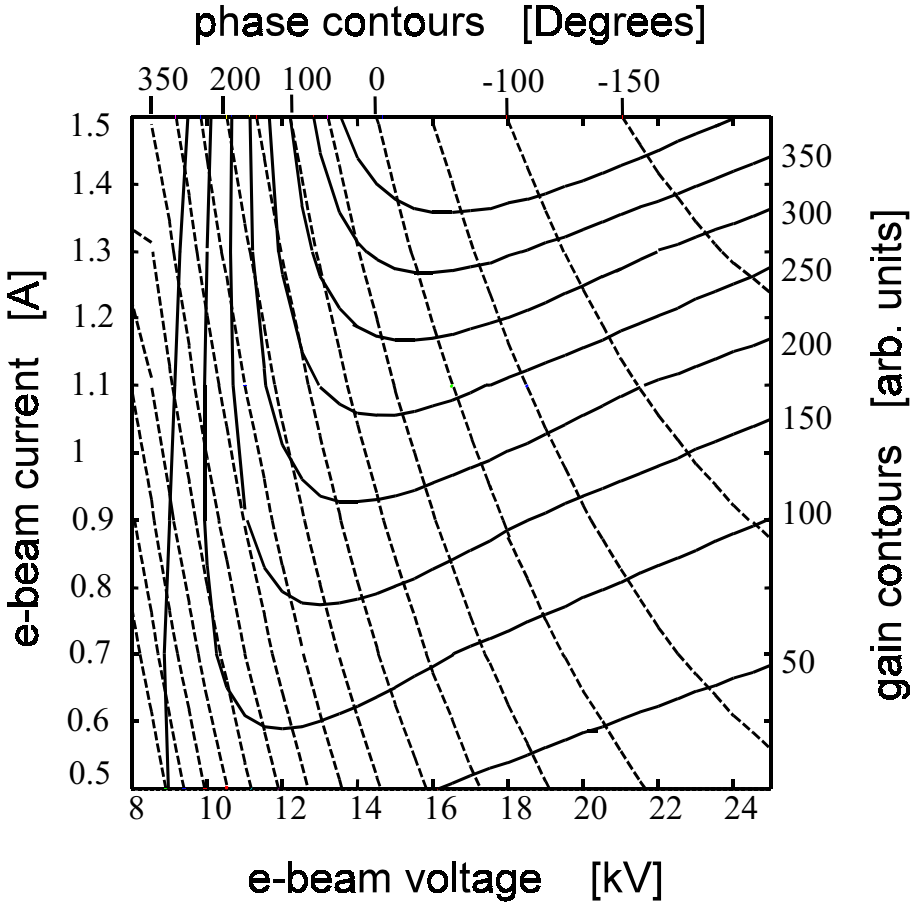

Figure 2.2: Gain and Phase contours of a single CRM-element for the parameters listed in Table 2.1. The solid and dashed lines are gain and phase contours, respectively, vs. the electron-gun voltage and current.

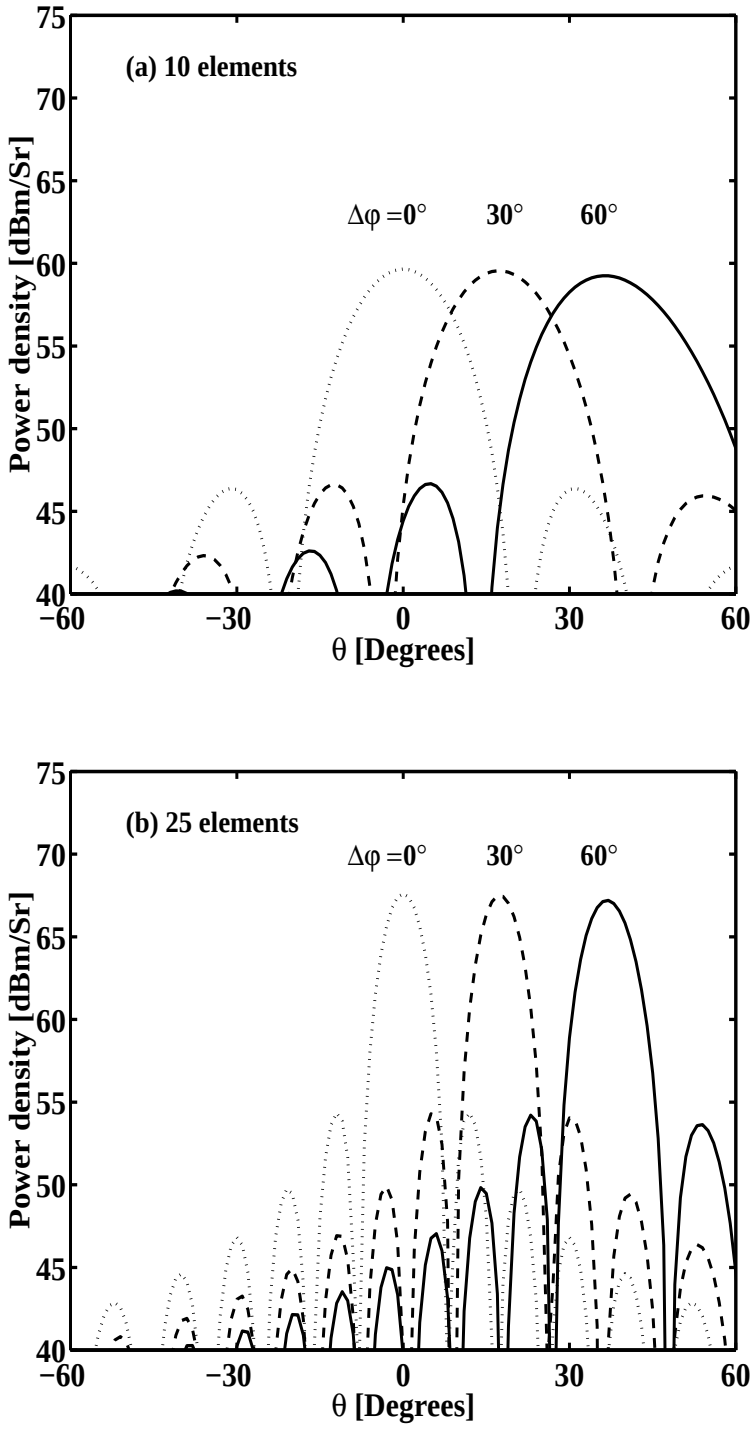

Figure 2.3: Radiation pattern for phase differences of 0°, 30° and 60° between the CRM-elements, for 10 (a) and 25 (b) elements.

2.3 Discussion

Radiation beam steering in the range of $\pm 35^\circ$ is demonstrated for an active antenna array from uncoupled CRM-elements. The low electron-beam voltage and current of each CRM-element are tuned between 10–24 kV and 0.7–1 A, respectively, to obtain a full 360° phase range with a constant gain.

These theoretical results are an important step towards feasible active CRM-array antennas. The high-power radiation is integrated in the far-field from the low-power CRM-element outputs, instead of a single high-power device. Thus, a compact device with steering abilities can be built by increasing the CRM dimensionality.

The next three chapters describe three types of low-voltage low-current CRM-elements applicable for the CRM-array antenna. These elements determine the characteristics of the CRM-array. In particular, the next chapter describes phase and gain measurements in a CRM-amplifier, with respect to its interaction parameters. The experimental results are compared to theoretical calculations, similar to those obtained in Fig. 2.2.

Chapter 3

Phase and Gain Measurements in a Distributed-Loss CRM Amplifier

3.1 Introduction

Output power, gain, and bandwidth are fundamental characteristics of CRM amplifiers. The feature of an inherent phase control in high-power amplifiers could be useful, in general, for several future applications of existing and novel devices. In particular, phase control is essential for the radiation beam-steering by CRM-arrays. This requires however a means to decouple the gain and phase variations (For instance, keeping the gain level fixed while varying

the phase delay.).

The concept of CRM-arrays and its implementations is presented in the previous chapter. A particular application for an array of CRM-amplifiers is the radiation beam steering, as an active phased-array antenna [20]. In this CRM synthesis, the simultaneous control of the gain and phase-delay of each CRM-amplifier-element is achieved by varying its electron-beam current and voltage. In such implementation the total radiated power is proportional to the number of CRM-amplifier elements in the array and to the output power of each element. The radiation pattern is shaped by the relative phase differences among the elements. If the control over the phase-delay could be an inherent feature of the CRM-amplifier, the need for external phase shifters could be alleviated. A similar angular steering method by free-electron laser (FEL) array proposed in Ref. [34] was demonstrated by Cecere and Marshall [37].

Another CRM application proposed by Granatstein and Lawson [38, 39] in which phase control could be essential is the use of gyro-amplifiers and gyroklystrons as RF sources for driving particle accelerators. Inherent CRM features of phase control and phase stability may play an important role in these future applications.

The investigation of phase-delay variations in CRM gyro-amplifiers is essential not only for their incorporation in future schemes, which require

inherent CRM phase-shifting abilities, but also for straight forward amplification purposes in which the phase stability is a major quality factor. Aspects of phase stability are studied in Refs. [40] and [41] for second-harmonic and frequency multiplying traveling-wave amplifiers, respectively.

Gyro traveling-wave amplifiers tend to oscillate, in particular in high-gain operation, but Chu *et al.* [42] showed that these oscillations can be suppressed by a lossy section along the waveguide. The distributed wall losses in this section decay the oscillations but maintain the CRM amplification, whereas the following non-lossy section extracts the high output power. Using this concept, Chu *et al.* have obtained an ultra high-gain (70 dB) at the Ka-band [10].

In order to study the applicability of Chu's amplifier scheme as an element of the phased CRM-array active antenna, the dependence of its gain and phase-delay on the operating parameters has been studied experimentally. The results are applicable for other possible applications as well.

This chapter presents a gyro-amplifier experiment implementing the distributed losses concept, in order to study its gain and phase-delay dependencies on the electron-beam current and the axial magnetic field. The objectives of this study are (a) to demonstrate phase variation experimentally, (b) to verify the experimental results with theory, and (c) to prove that the gain and phase-delay can be controlled independently, as predicted in Ref. [20].

The results of this chapter are published in Ref. [21].

Table 3.1: Experimental operating parameters

Electron beam voltage	18	kV
Electron beam current	0.25–0.4	A
Kicker pitch-ratio	1.3	
Pitch-ratio spread	7–12	%
Solenoid magnetic field	~ 2.5	kG
Cyclotron harmonic number	1	
Waveguide cross-section	23×10	mm^2
Interaction length	100	cm
Lossy section length	76	cm
Loss factor	5	Np/m
Frequency	~ 7.3	GHz

3.2 Experimental setup

The CRM experimental scheme is shown in Fig. 3.1. The experimental operating parameters are listed in Table 3.1. A linear electron-beam is generated by an electron-gun based on a thermionic cathode (Heatwave STD200). A cylindrical plate with a 5 mm diameter through-hole is placed 5 mm from

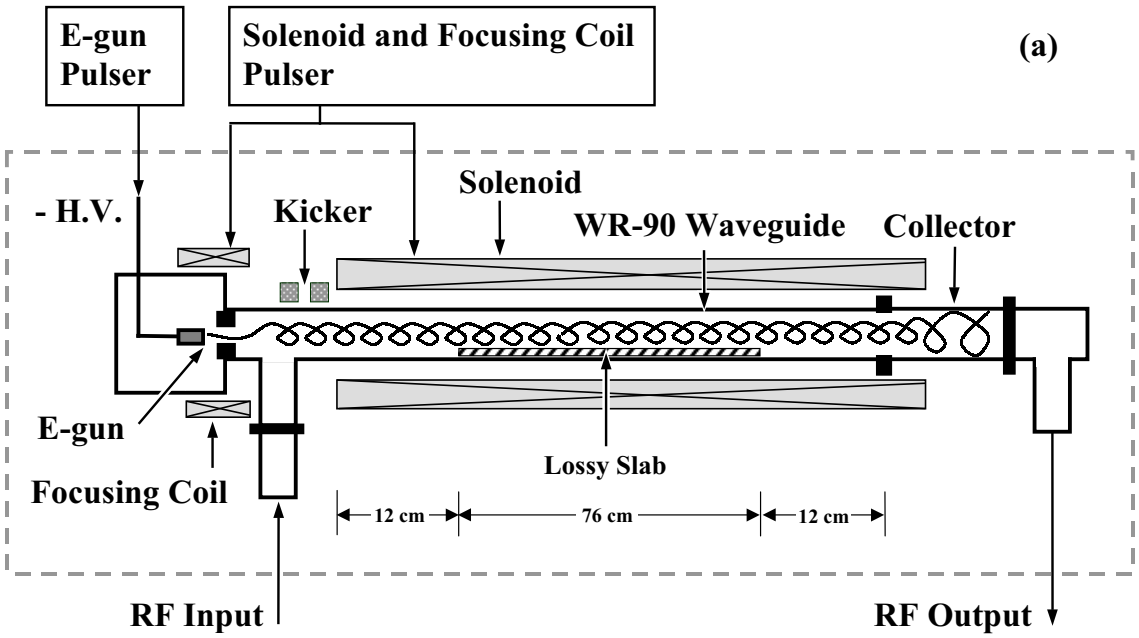

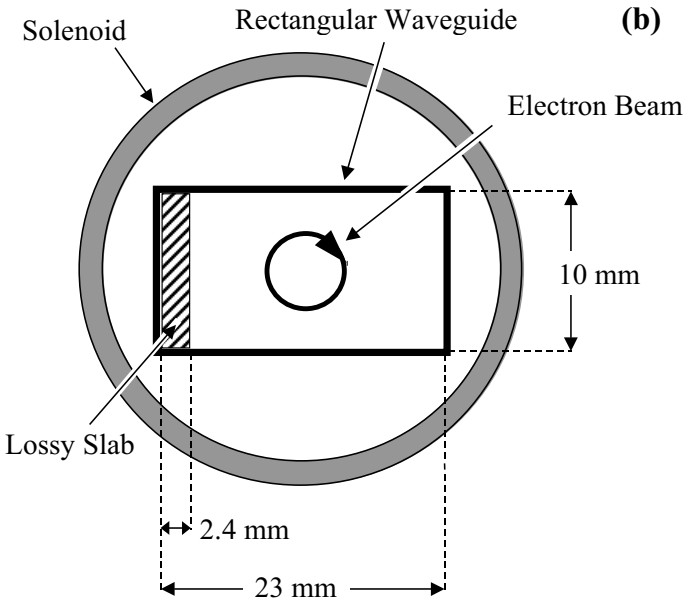

Figure 3.1: The CRM experimental scheme (a), and a cross section in the lossy waveguide section (b).

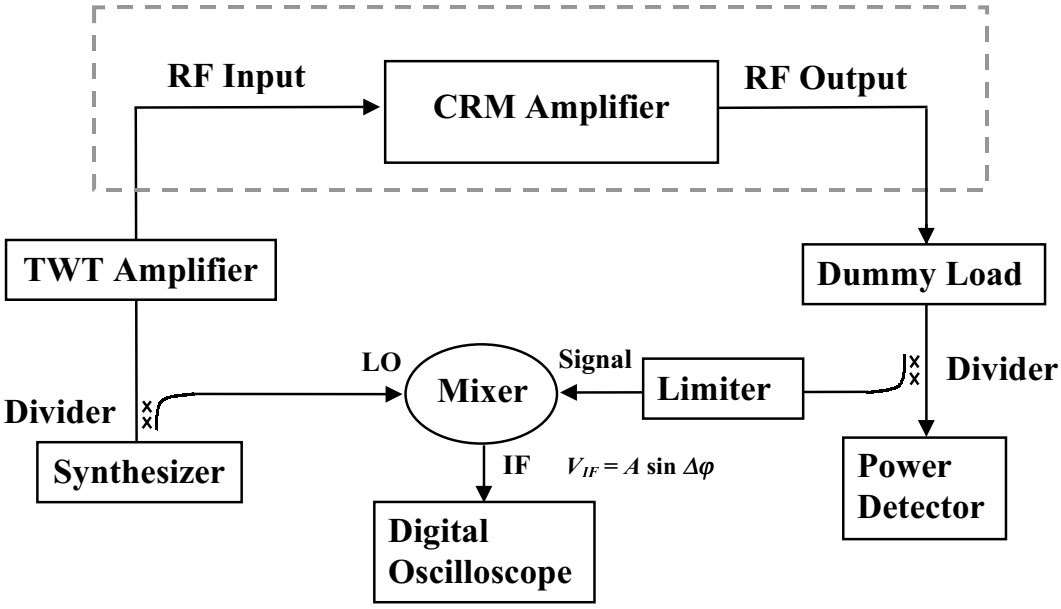

Figure 3.2: Microwave diagnostic setup.

the cathode to serve as an anode. The beam is focused by a focusing coil into the kicker section. The kicker consists of two plates of Neodymium Iron Boron (NdFeB) permanent magnets. The magnets are attached to the wide waveguide face and are poled into and out of it in the transverse direction. This kicker configuration resembles a wiggler's half period [43]. The electron gun and kicker are designed by the Herrmannsfeldt EGUN simulation code [44]. The electron beam pitch-ratio is found to be $\alpha \cong 1.3$ with a spread of $\Delta\alpha/\alpha \cong 12\%$. The beam is rotating in the cyclotron frequency along the axis of the WR-90 rectangular waveguide. The axial magnetic field is produced by a 1.1-m long solenoid.

The 1-m interaction length is succeeded by a 0.1-m waveguide extension

operating as a collector. A lossy section of a 76 cm long graphite slab (10.0×2.4 mm^2 cross section) is located in the center part of the interaction region, as shown in Fig. 3.1(a). A transverse cross section of the CRM across the lossy waveguide section is shown in Fig. 3.1(b). The slab is attached to one of the narrow waveguide walls in order to suppress backward-wave CRM oscillations [45]. The waveguide insertion loss due to the lossy slab is 35 dB at the 7.3 GHz operating frequency.

The electron-gun is fed by a 19 kV pulse generator. The solenoid and focusing coil are connected in series and fed by a current pulser. The maximal axial magnetic field is 2.7 kG, obtained in a pulse duration of ~ 4 ms.

The microwave diagnostic setup is shown in Fig. 3.2. The input signal (7.3 GHz, 1.6 W) is pulse modulated (6 μs pulse period, 80% duty cycle). It is produced by a synthesizer (HP 83752A) connected through a power divider to a TWT amplifier (Varian VZC-6960H1) and injected into the RF input port of the CRM. The input signal modulation enables one to verify at the output stage that the CRM operates indeed as an amplifier and that it does not oscillate.

The amplified output signal is dumped by a dummy load. A sampling of the output signal is split by a two arm power divider. One arm is connected to a crystal power detector (HP 423B) to measure the output power. The other arm is connected through a power limiter (MW-16300-SF-SF) to the

signal port of a mixer (Magnum Microwave MM134P-1). The LO port of the mixer is fed by the RF synthesized generator (as shown in Fig. 3.2). The mixer IF output port voltage V_{IF} corresponds to the CRM phase delay by

$$V_{IF} = A \sin \Delta\varphi(t), \tag{3.1}$$

where A is a constant and $\Delta\varphi(t)$ is the time-dependent CRM phase delay. In this experiment the CRM phase-delay is derived from the mixer output trace.

3.3 Experimental results

The CRM experimental setup described above was operated with the parameters listed in Table 3.1. The measured beam voltage and current are 18 kV and 0.3 A, respectively. Figs. 3.3(a-c), show for instance, raw measurements of the solenoid field, the power detector, and the mixer output waveforms, respectively. It can be seen that during a 30 G fall of the solenoid field, the output power varies from 57 to 48 dBm, and the mixer IF output (3.1) accumulates one period of a sine wave. The power detector and mixer outputs are pulse modulated as the input signal, indicating a CRM amplification with no oscillations.

Figs. 3.4(a-d), show accumulated experimental results indicating the dependencies of the power gain on the beam voltage, beam current, signal

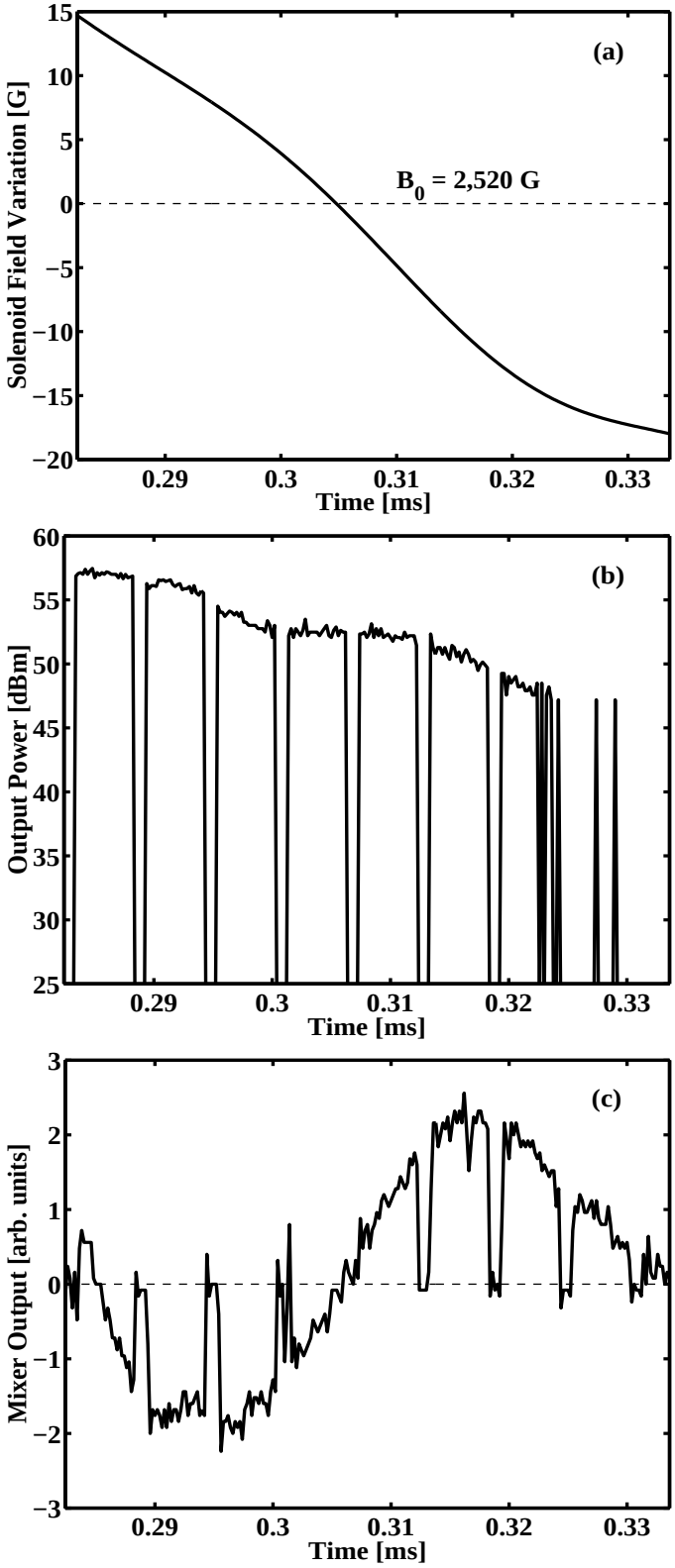

Figure 3.3: Waveforms versus time of the axial magnetic field (a), output power (b), and mixer output (c).

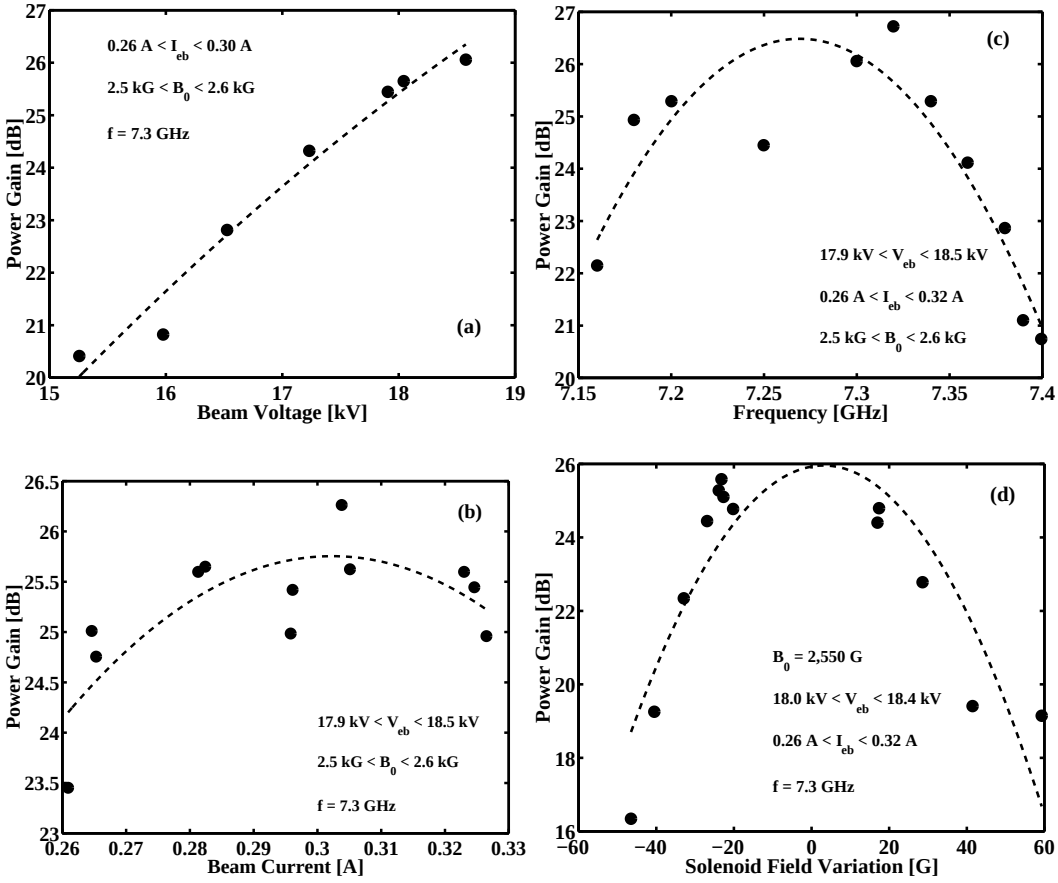

Figure 3.4: Measurements of the power gain with respect to beam voltage (a), beam current (b), signal frequency (c), and solenoid field (d). The dots indicate the maximum gain obtained within the parameter ranges shown, and the dashed curves are their calculated second-order fits.

frequency, and solenoid field, respectively. The operating parameters are indicated in each figure by their specific ranges, whereas the common parameters are as listed in Table 3.1. The dots indicate the maximum gain obtained within the specified parameter ranges. The dashed curves represent the second-order fit approximations of the experimental results. Fig. 3.4(a) shows the linear tendency of the gain to increase with the beam voltage. Fig. 3.4(b) shows that the gain attains a maximum for beam currents near ~ 0.3 A. Fig. 3.4(c) shows the gain curve with respect to the signal frequency in the range of 7.15 to 7.40 GHz. Fig. 3.4(d) shows the complementary dependence of the gain on a slight variation in the solenoid field in a fixed frequency (7.3 GHz). Both Figs. 3.4(c,d) indicate a tuning bandwidth of $\sim 2.5\%$ for this CRM amplifier.

The experimental study of the CRM phase variation is supported by a theoretical analysis of the combined phase and gain dependencies on the solenoid field and e-beam current. This simultaneous dependence is calculated theoretically using the CRM nonlinear differential equations given in Ref. [46]. These equations are solved by the fourth-order Runge-Kutta method along the interaction axis for the CRM parameters listed in Table 3.1. The intermediate lossy section is presented by an imaginary component ($k_z'' = 5$ Np/m) added to the axial wavenumber in order to simulate the waveguide distributed loss. The computed theoretical results are plotted in Fig. 3.5

as gain contours (solid lines) and phase-delay contours (dashed lines) versus the e-beam current and solenoid field. The theoretical results show that a full 360° phase-delay range is achievable over a limited range of equi-gain contours.

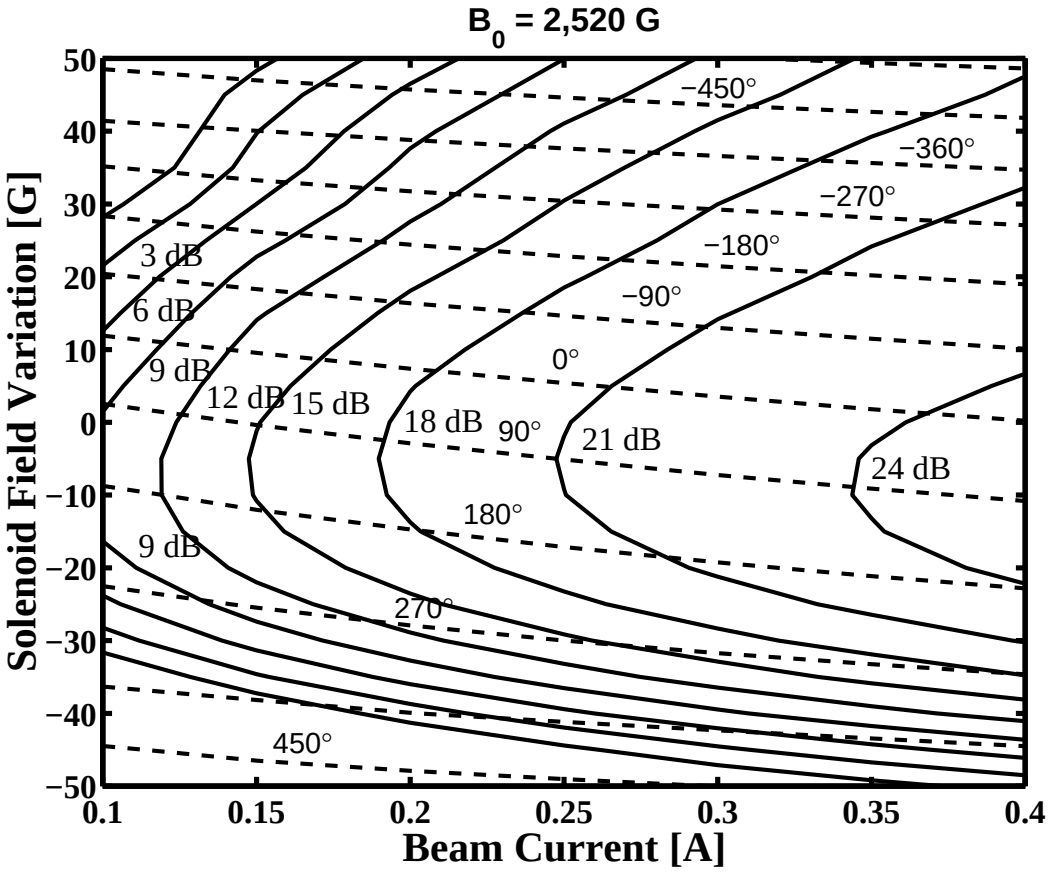

Figure 3.5: A theoretical non-linear computation of the CRM gain (solid contours) and phase-delay (dashed contours) versus the e-beam current and solenoid field variations around 2,520 G. The operating parameters are listed in Table 3.1.

Experimental measurements of the phase-delay dependence on the solenoid field are shown in Fig. 3.6 for a CRM gain of 19.5 ± 0.5 dB and a 320 ± 5 mA e-beam current. A phase variation of 0–180° is demonstrated in these conditions. The dashed line shows, for comparison, the theoretical results derived from Fig. 3.5 for the same conditions.

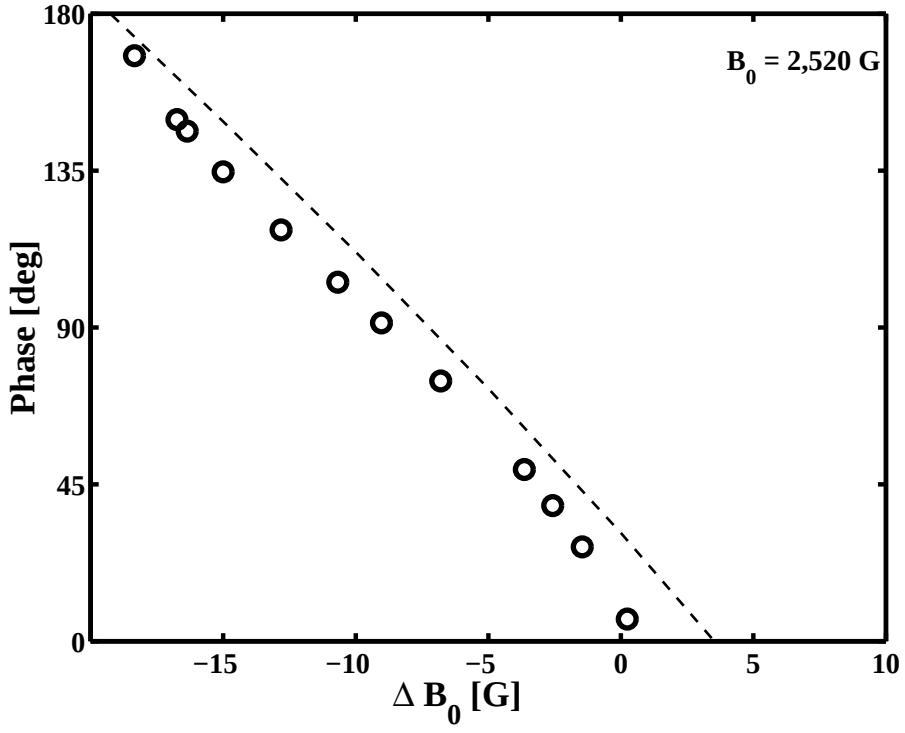

Figure 3.6: Phase-delay measurements vs. solenoid field for a 19.5 ± 0.5 dB gain and 320 ± 5 mA e-beam current. The dashed line shows the theoretical result derived from Fig. 3.5 for the same conditions.

A full-cycle phase variation (0–360°) is demonstrated experimentally in Fig. 3.7 for a fixed gain (23.5 ± 0.5 dB) and a compensating e-beam current

(320 ± 40 mA) and voltage (18 ± 1 kV). The three-dimensional graph in Fig. 3.7 shows experimental results (circles) and their second-order best fit projections on the three perpendicular planes of this figure (in solid lines). For a comparison with the theoretical model, the corresponding computation results presented in Fig. 3.5 are shown with the experimental results of Fig. 3.7. The dashed curves on the $\Delta\varphi - I_{eb}$, $\Delta\varphi - \Delta B_0$ and $I_{eb} - \Delta B_0$ planes show these theoretical results. A considerable agreement between experiment and theory is acknowledged.

In view of recent advances in gyro-TWT studies for radar applications [47], there is an interest to characterize the features of this CRM amplifier in parametric terms related to radar and communication engineering. These characteristics include amplitude and phase modulation coefficients, spectral purity, phase linearity, and output noise, as investigated in Ref. [48]. In our CRM experiment, the amplitude modulation (AM) coefficients for the beam-current and solenoid-field variations are obtained from Figs. 3.4(b,d) as ~ 0.12 dB/% and ≤ 5 dB/%, respectively. These experimental outcomes agree with the theoretical result derived from Fig. 3.5.

The phase modulation (PM) coefficient for the beam current variation is derived theoretically from Fig. 3.5 as $0.9^\circ/\%$. The PM coefficient for the solenoid field variation is derived from the experimental results in Figs. 3.3(a,c), as $220^\circ/\%$, in agreement with the theoretical result from Fig. 3.5. Theoretical

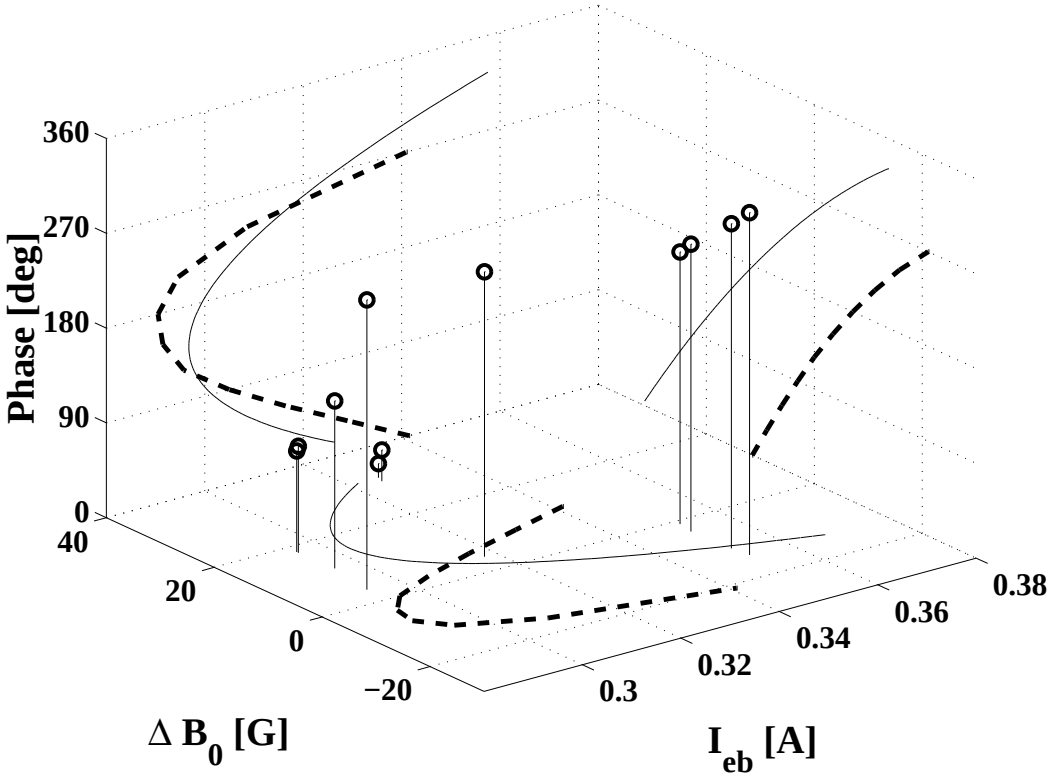

Figure 3.7: Phase-delay measurements (shown by circles) vs. e-beam current and solenoid field for a 23.5 ± 0.5 dB gain. The solid curves on the perpendicular planes show the second order best fits of the experimental results projections. The dashed curves show the theoretical results derived from the CRM model in Fig. 3.5 for the present conditions.

calculations of the CRM's bandwidth and phase linearity show an immediate bandwidth of 150 MHz (between -3 dB points), and a phase variation of $\pm 7^{\circ}$ from the best-fit linear phase line within this frequency range.

Spectral purity measurements were obtained by mixing the CRM output signal (7.3 GHz, CW) with a local-oscillator signal at 7.35 GHz. The mixer IF output sampling was transformed to the frequency domain by a discrete Fourier transform (DFT). The spectral widening at the -10 dB points was found to be $\leq$ 40 kHz with respect to the spectral width of the setup itself (230 kHz). The output noise, measured by a spectrum analyzer (HP 8592A) in the CRM's output port while the input port was terminated by a dummy load, was found to be -22.5 dBm/MHz. This yields a 65.5 dB noise figure for the CRM's 26 dB gain.

3.4 Discussion

In this experiment, a distributed loss CRM-amplifier [42] is operated at 7.3 GHz, with an 18 kV, 0.3 A electron beam. A maximum gain of 26 dB is obtained with an 0.63 kW output power, and a 12% non-saturated efficiency. This experiment extends the validity of the CRM distributed-loss concept to another operating regime than presented originally by Chu *et al.* [10, 42].

Furthermore, the feasibility of uncoupled gain and phase-delay variations

in a CRM-amplifier is demonstrated experimentally. A full 360° phase-delay variation for a fixed CRM gain is obtained experimentally, in agreement with theory (see Fig. 3.7). This result demonstrates in principle the feasibility of a phased-array active CRM antenna made of uncoupled distributed-loss CRM amplifier elements. Such an array requires a 360° variation range of an inherent CRM phase-shift with an independently controlled gain [20]. This feature is demonstrated successfully in this experiment.

The simultaneous controllability of the phase-delay by the electron beam current and by the solenoid magnetic field is demonstrated experimentally and theoretically. Both agree within $\sim 4\%$ in the electron beam current and $\sim 1\%$ in the solenoid magnetic field, and within a ± 0.5 dB gain margin. The electron pitch-ratio and spread values were not measured in this experiment. In the CRM computation we assumed electron pitch-ratio and spread of $\alpha = 1.3$ and $\Delta\alpha/\alpha = 7\%$, respectively, though the EGUN simulations predicted the same pitch-ratio with a higher spread ($\Delta\alpha/\alpha = 12\%$). This discrepancy has to be resolved in a future study.

The CRM amplifier characteristics such as amplitude and phase modulation coefficients, spectral purity, and phase linearity are evaluated in this study to be in a similar order of magnitude to the gyro-TWT scheme investigated by Ferguson *et al.* [48], but the noise figure found in our experiment is $\sim$ 15 dB higher. Hence, these preliminary characteristics should be im-

proved in order to enable the implementation of this CRM-amplifier scheme for radar and communication applications.

The gain and phase of the CRM amplifier, controlled here by the e-beam current and solenoid field, can be implemented in practice as well. For instance, the e-beam current can be controlled by a triode electron-gun. Means to tune the static magnetic field can be incorporated even with permanent magnets [49, 50], or in super-conducting magnets [51]. In these CRM schemes, a magnetic field variation in the order of 1% is required for a full 360° cycle. This can be achieved by an additional low-current solenoid. In other CRM schemes, gain and phase controls can be implemented by the e-beam voltage [20] or by the electron pitch-ratio variations.

The control over the phase delay could be essential as well for high-power gyroamplifiers and gyroklystrons designed to drive TeV linear colliders [38, 39]. This feature could be used for an in-phase particle acceleration, to decrease phase jittering, and to stabilize CRM amplifiers.

Phase-controlled CRM-amplifiers can be integrated in CRM-arrays and operate as active phased-array antennas for high-power radars. The amplified signal can be radiated directly from each CRM-element aperture, while the proper phase and gain of each element are controlled by its electrical operating parameters, without the need for external (passive) phase-shifters.

Chapter 4

Feedback-Controlled CRM Oscillators

4.1 Introduction

Signal locking for CRM oscillators in general and for gyrotrons in particular are used in order to control their performance. Different locking methods are used to increase the stability and coherence of the oscillator, control its frequency, and to obtain modulations.

Mode locking by modulating the axial velocity of the electron beam in a closed cavity gyrotron was analyzed and simulated in Refs. [52, 53] to produce a train of narrow pulses with repetition of the modulation frequency. Improved phase locking by using a modulated electron beam was demon-

strated in a gyroklystron oscillator. The amount of power needed for obtaining the phase locking was decreased by more than an order of magnitude from that predicted by Adler's theory [54]. Frequency control and tunability were demonstrated in a gyro-BWO by injection locking through the down-stream port (near the collector). The oscillation power was extracted at the up-stream port (near the electron-gun) [55]. These methods requires an external source to drive the locking signal.

In free-electron laser (FEL) oscillators, periodic intensity bursts during the startup phase were observed and studied in Refs. [56]. The FEL's output port was coupled back into the input port by an external feedback waveguide. The micro-pulse period was related to the RF round-trip time and its width was related to the waveguide dispersion and the FEL slippage time [57].

Amplitude-modulation mode locking of a FEL oscillator was demonstrated by modulating the attenuation of the FEL ring cavity by a PIN diode [58]. The micro-pulse period was equal to the modulation period which was tuned to match the RF round-trip time.

This chapter presents experimental results of pulse and frequency modulation of a CRM oscillator by an external feedback-control. Its principle scheme is shown in Fig. 4.1. It consists of a CRM amplifier employing a distributed-loss waveguide to prevent backward-wave oscillations [10]. A coupling of its output is connected through a controlled feedback to its input port. The

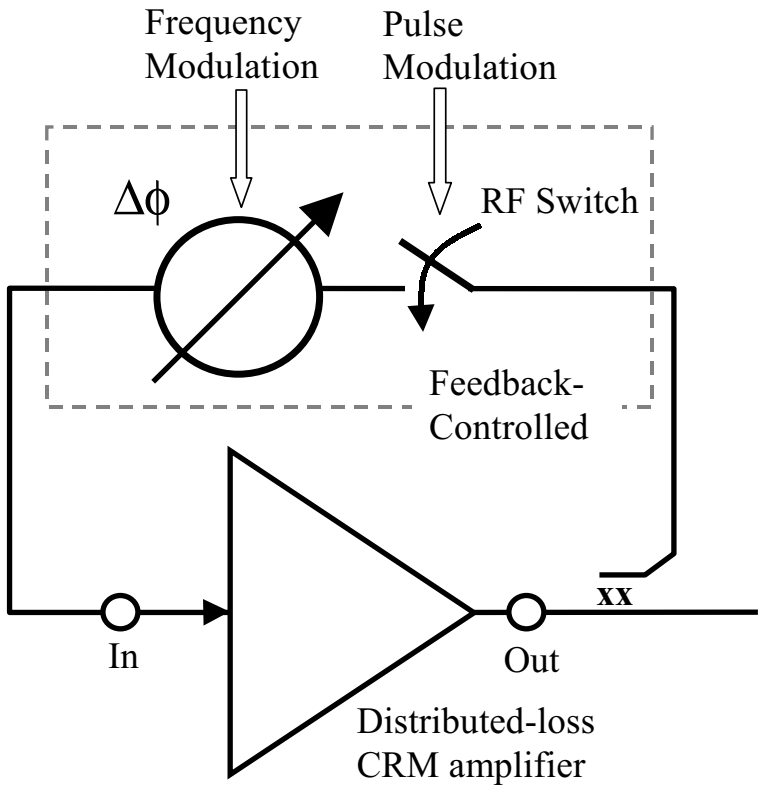

Figure 4.1: Basic principle of amplitude and frequency modulation by a feedback-controlled oscillator

feedback-controlled consists of an RF switch and a phase-shifter.

The RF switch closes and opens the feedback loop, thus, its modulation can cause corresponding pulse modulation at the oscillator output. The phase-shifter changes the accumulated phase along the feedback loop, thus, its modulation can cause corresponding frequency modulation at the output. The permitted oscillation frequencies, f_n, of the closed-loop oscillator are

those who satisfy

$$\Delta\phi + 2\pi f_n \tau_{loop} = 2\pi n \tag{4.1}$$

where the shifter phase is $\Delta\phi$ and

$$\tau_{loop} = \sum_i \frac{L_i}{V_{gr,i}(f_n)} \tag{4.2}$$

is the total round-trip time delay, along the loop components with physical length and group velocity L_i, and $V_{gr,i}$, respectively. In Eq. (4.1) n is an integer number denoting the permitted discrete frequencies for a given phase-shift. These permitted frequencies are bounded within the CRM amplifier bandwidth.

The maximum modulation depth is achieved by modulating $\Delta\phi$ in the range of $0 - \pi$. Therefore, the maximum modulation depth, by Eq. (4.1), is

$$\Delta f_{max} \cong \frac{1}{2\tau_{loop}} \,. \tag{4.3}$$

The objective of this chapter is to demonstrate the ability to obtain pulse or frequency modulations by feedback-control. This method does not require an external driving source. The control is used at the low power level of the CRM-amplifier input. Such schemes of pulse and frequency modulation could be used in radar applications.

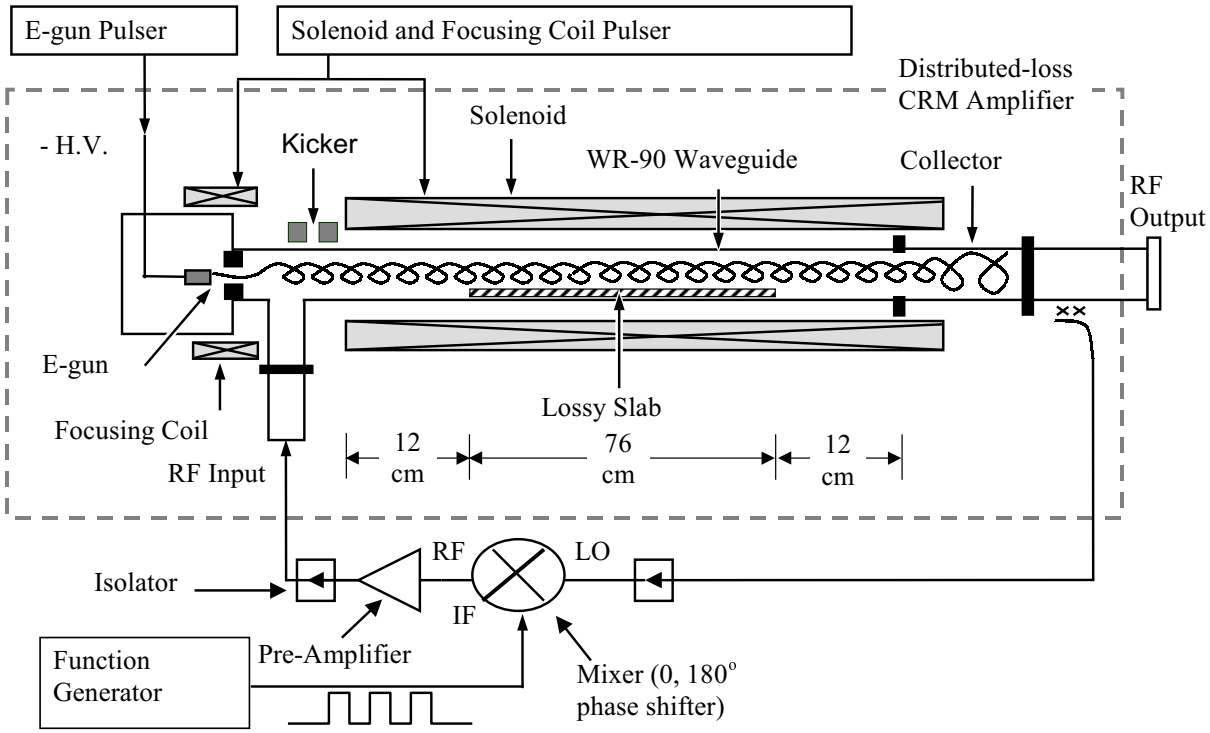

Figure 4.2: Controlled feedback CRM oscillator experimental setup. The mixer serves both for modulating the amplitude and phase-shift of the feedback.

4.2 Experimental setup

The distributed-loss CRM amplifier is described in details in Chapter 3. The experimental scheme of the feedback-controlled CRM oscillator is shown in Fig. 4.2. The experimental operating parameters are listed in Table 4.1.

The output signal is coupled to the CRM amplifier input port through a coupler, a 2-m transmission line, isolators, a mixer (Stellex M79HC) and a pre-amplifier (Varian VZC-6960H1 traveling-wave tube), as shown in Fig. 4.2.

Table 4.1: Experimental operating parameters

Electron beam voltage	15.4	kV
Electron beam current	0.28	A
Kicker pitch-ratio	1.3	
Pitch-ratio spread	12	%
Solenoid magnetic field	~ 2.4	kG
Cyclotron harmonic number	1	
Waveguide cross-section	23×10	mm^2
Interaction length	1	m
Lossy section length	0.76	m
Loss factor	5	Np/m
Feedback modulation frequency	0.1	MHz

The TWT pre-amplifier is used in order to drive the CRM by a 1.6 W input power. The time delay of the feedback components is ~ 25 ns, in which 12 ns are due to the transmission line and the passive components, and 13 ns are due to the TWT pre-amplifier.

The calculated time-delay and instantaneous bandwidth of the CRM-amplifier are 17 ns and 150 MHz, respectively. Therefore, the calculated setup τ_{loop} is 42 ns, which corresponds to maximum modulation depth of

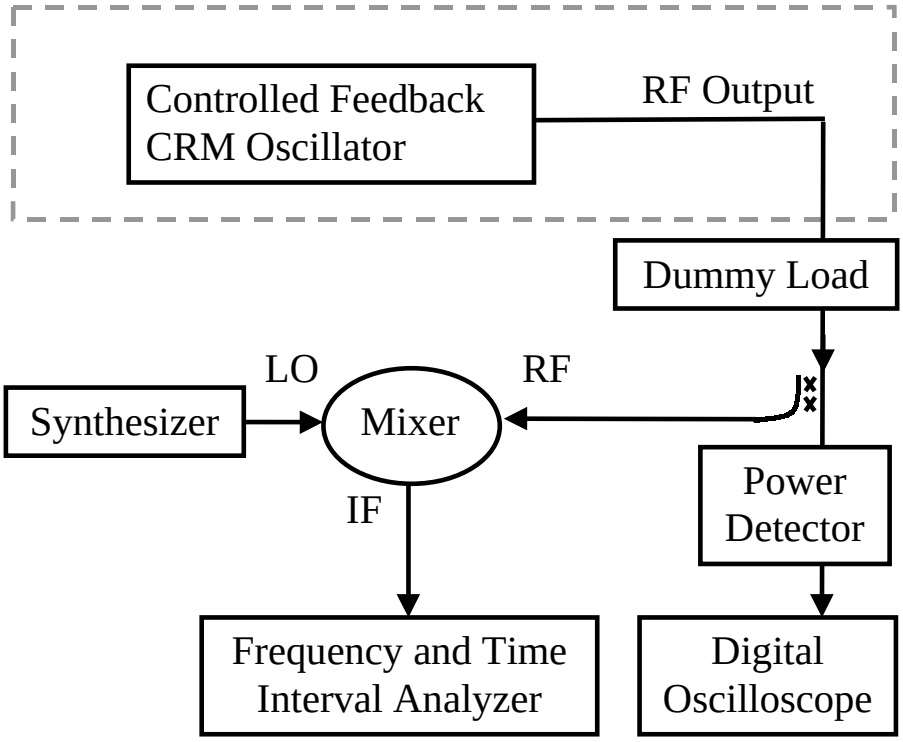

Figure 4.3: Microwave diagnostic setup.

12 MHz. Since the maximum modulation depth is less than the instantaneous bandwidth, the device is subjected to oscillate in several discrete frequencies, f_n, within the bandwidth.

The mixer serves as both an RF switch and as a 0/180° phase shifter (this is a non-conventional operating mode of mixers controlled by the IF port [59, 22]). Its insertion loss is high when no signal is present at its IF port, thus the feedback loop is 'opened'. A positive or negative DC signal at its IF port shifts its RF port by 0° or 180° with respect to its LO port, respectively. The IF port is connected to an arbitrary-wave function generator (HP 33120A).

The function generator is set to produce a three-state waveform: positive, zero, and negative, as shown in Fig. 4.4(a). This particular waveform was chosen in order to modulate the mixer between its three states during the solenoid sweep.

The second arm of the coupler at the RF output port is connected to a diagnostic setup as shown in Fig. 4.3. The setup includes a dummy load connected to a power detector (HP 423B) and a coupling to a mixer (Magnum Microwave MM134P-1). The mixer LO port is connected to a synthesizer (HP 83752A) and its IF port to a frequency and time interval analyzer (HP 5372A) for frequency measurements. The synthesizer frequency was set to 7.8 GHz which is above the oscillating frequencies.

4.3 Experimental results

The controlled feedback CRM oscillator described at the experimental setup section was operated with the parameters listed in Table 4.1. The measured beam voltage and current are 15.4 kV and 0.28 A, respectively.

Fig. 4.4(a) show raw measurement of the mixer IF signal. Fig. 4.4(b) show the corresponding raw measurements of the detected output power. It can be seen that its trace is modulated according to the mixer IF voltage. The power is 'on' when the IF signal is positive or negative, and 'off' when the

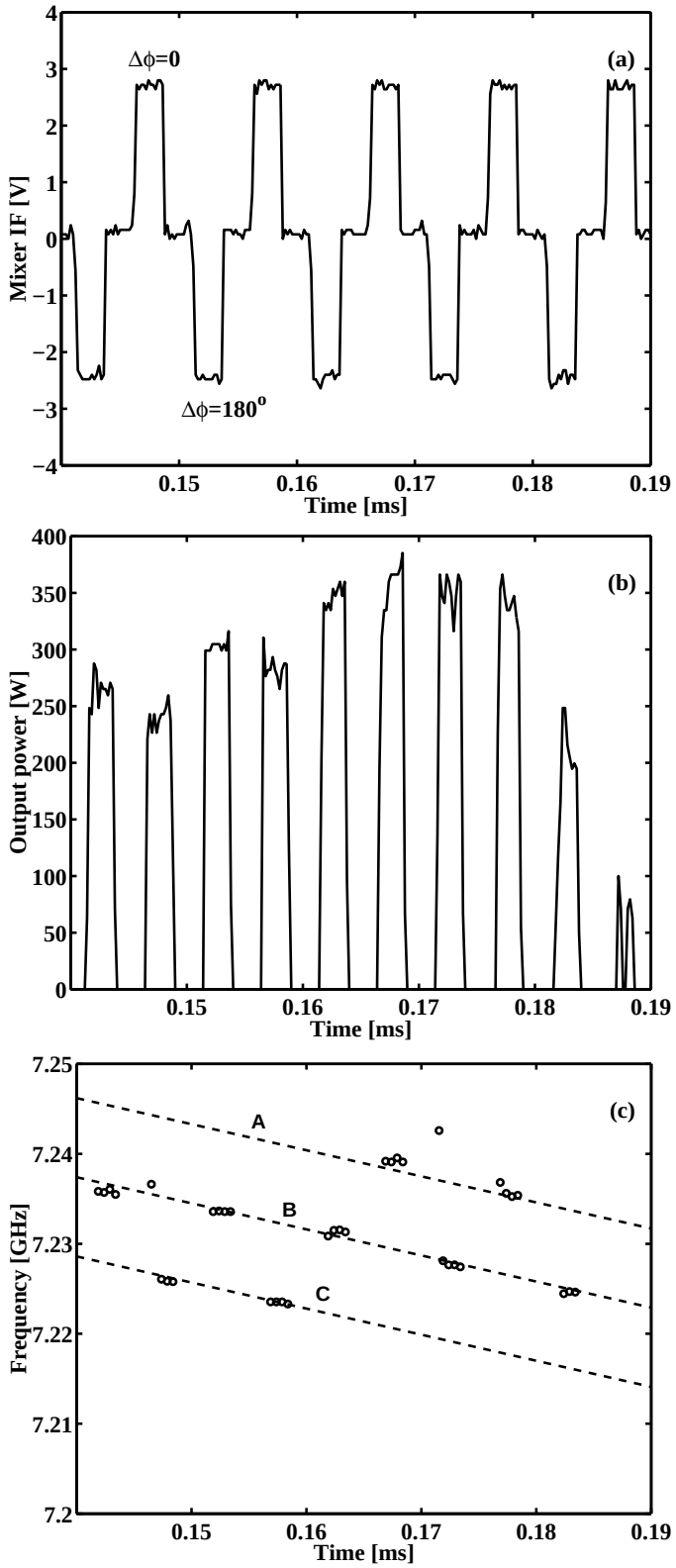

Figure 4.4: Waveforms versus time of the modulation at the mixer IF port (a), solenoid current (b), power detector voltage (c), and measured frequency (d).

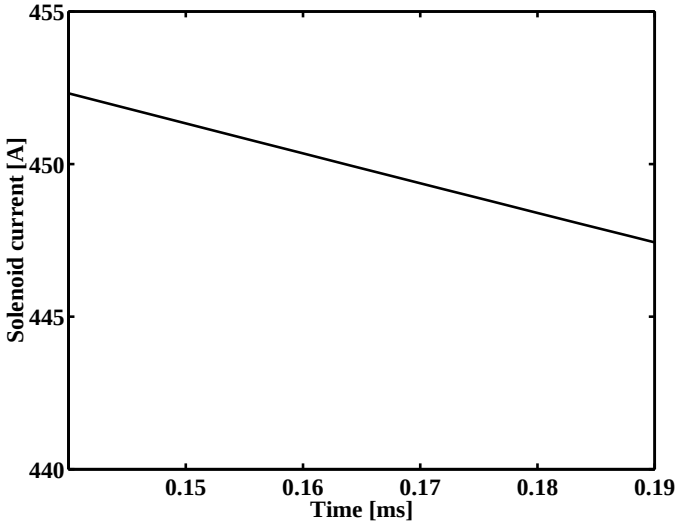

Figure 4.5: The solenoid current waveform versus the time shown in Fig. 4.4.

IF signal is zero. The measured oscillation power at the 'on' state is 370 W. Thus, the CRM operates as an amplifier, and is not subjected to backward-wave instabilities. The pulse modulation oscillation mode is obtained by controlling the feedback insertion loss.

Fig. 4.4(c) shows the corresponding raw measurement of the frequency where the circles indicate the frequency levels when the mixer IF signal was positive or negative. It can be seen that the CRM oscillates around ~ 7.23 GHz, and is frequency modulated according to the feedback phase-shifting determined by the mixer. These frequency points are located on three major dashed lines denoted as 'A'–'C'. These three lines are separated by 8.8 MHz frequency shifts. It is seen that the frequency points on the 'A' and 'C' lines correspond to $\Delta\phi = 0$, while the points on the 'B' line corre-

spond to $\Delta\phi = 180°$. Furthermore, the frequency point located consequently on the 'B' and 'C' lines are between 0.140–0.165 ms, while those on the 'B' and 'A' lines are between 0.165–0.85 ms. Thus, these lines are regarded as the permitted frequencies in Eq. (4.1), where the 'A' and 'C' lines correspond, for example, to $\Delta\phi = \pm 180°$ and f_n changes to f_{n+1}.

The round-trip time was measured by sampling the round-trip power at two locations: before the mixer LO port, and after the TWT pre-amplifier output. The time delay of the sampled signals was compared with respect to the fall to their 'off' states (a measurement with respect to the 'on' state might be incorrect due to oscillation buildup time). The measured time delay is 65 ns, where the 13 ns of the TWT pre-amplifier are added to yield a total measured round-trip time of $\tau_{loop} = 78$ ns. This time corresponds to a maximum modulation depth of 6.4 MHz, which is in the order of the measured 8.8 MHz and the calculated 12 MHz.

Fig. 4.5 show raw measurement of the solenoid current during the time shown in Fig. 4.4. The solenoid current is proportional to the axial magnetic field. It is seen that the 'A'–'C' lines in Fig. 4.4(c) have a slight slope, together with the fall of the solenoid current. The sensitivity of the CRM amplifier phase-shift to the axial magnetic field was measured in Chapter 3 and is in the order of 220°/%. It is seen that the solenoid current falls 1.22% which corresponds to a 270° phase-shift. Such phase-shift corresponds to

13.2 MHz frequency shift, which agrees with the 14 MHz frequency fall of each line.

4.4 Discussion

Experimental results of both pulse and frequency modulations are demonstrated by oscillating a CRM amplifier through to a controlled feedback. The CRM oscillator is operated at 15.4 kV, 0.28 A electron beam. The oscillating frequency is obtained around 7.23 GHz, and the output power is 370 W which corresponds to interaction efficiency of 9%. These parameters are close to those obtained for the CRM-amplifier described in Chapter 3

A mixer at the feedback served both as a controllable RF-switch and as a 0/180° phase shifter. The pulse modulations were obtained by controlling the mixer insertion-loss, while the frequency modulations were obtained by controlling its phase-shift. In practical applications, these features could be separated according to the required modulation.

The two phase-shifting states of the mixer enabled to modulate the frequency between two corresponding levels of 8.8 MHz apart. Thus, a frequency-shift keying (FSK) modulation is obtained by this mixer. The solenoid sweep obtained due to its pulsed operation enabled to sweep the frequency modulations in a continuous range. This sweep agrees with the phase sensitivity

described in Chapter 3. A digital phase-shifter is a practical possibility for stepped- or linear- frequency-modulation (SFM or LFM).

The 6.4 MHz maximum modulation depth derived from the measured round-trip time delay is in the order of the 8.8 MHz modulation depth shown in Fig. 4.4(c). In order to increase the maximum modulation depth, the round-trip time delay should be decreased. Frequency ambiguity between lines 'A' and 'C' would be disabled if the modulation depth is wider than the CRM amplifier instantaneous bandwidth.

Such method of feedback-controlled does not require an external local-oscillator to obtain the pulse and frequency modulations. The feedback is controlled at low-voltage levels of ± 2.7 V at the mixer IF port. The signal is injected through the CRM amplifier RF input port, thus, its input level can be low as long as the open-loop gain is above one.

This method might be attractive for high-power radar applications. The modulation rate, determined by the mixer IF signal, is limited mostly by the modulator itself, and by the rise time of the CRM oscillations. This rise time is related to the round-trip time and to the open-loop gain before saturation. The rise-time was not measured in this experiment, however the mixer switching rate was 0.2 MHz.

The approach of controlling oscillations by the external feedback might be important for other applications, such as stabilizing and tuning the os-

cillation frequency by controlling the feedback-phase. It can also be used to drive in-phase several high-power oscillators in general, and a CRM-array in particular, and obtain a power summation from all of the array elements.

Chapter 5

Ferrite-Guided CRM

5.1 Introduction

The CRM interaction involves two competing physical mechanisms of the *em* wave with the helical orbiting electron-beam in the axial magnetic field [60]. The first mechanism originates from the relativistic dependence of the cyclotron frequency on the electron energy. This effect induces the azimuthal phase bunching of the orbiting electrons. The opposite mechanism is the axial bunching effect, caused by the axial velocity modulation of the electrons (this effect is known also as the Weibel interaction).

The azimuthal bunching mechanism dominates in fast-wave devices. For instance, gyrotron devices [9] utilize highly azimuthal bunching due to their large *em* phase-velocity (near waveguide cutoff). Gyrotron's record exceed

up to a 850 GHz frequency [61] and up to a 70 dB amplifier gain [10]. The latter achievement is made feasible by a distributed loss along the interaction, which suppresses the undesired backward waves.

The axial bunching mechanism dominates in slow-wave CRM's. Such devices, with dielectric loads [62, 63] and periodic waveguides [64, 65] were demonstrated experimentally. The dielectric load or the periodic structure (i.e. artificial dielectric) decreases the impedance of the *em* wave involved in the azimuthal bunching, and enhances the opposite axial bunching effect which may dominates then. The anomalous Doppler CRM effect [66, 67] may occur in these conditions. This effect enables for instance amplification even with a zero initial transverse velocity component of the electrons [36]. This feature alleviates the need for an initial kicking of the electron-beam, and it may simplify the CRM device operating in the anomalous regime.

This chapter proposes a concept of a CRM interaction incorporated in a ferrite-loaded waveguide [68]. Ferrite loads were discussed already in the early 60's for backward-wave tubes [69, 70]. In the presently proposed CRM, the ferrite loading slows down the wave phase-velocity and enhances the magnetic field component of the *em* wave involved in the axial bunching effect. Unlike periodic or dielectric loads for slow-wave CRM's, the ferrite permeability is a resonant effect governed by the same axial (static) magnetic field incorporated in the CRM device itself. The linear model presented

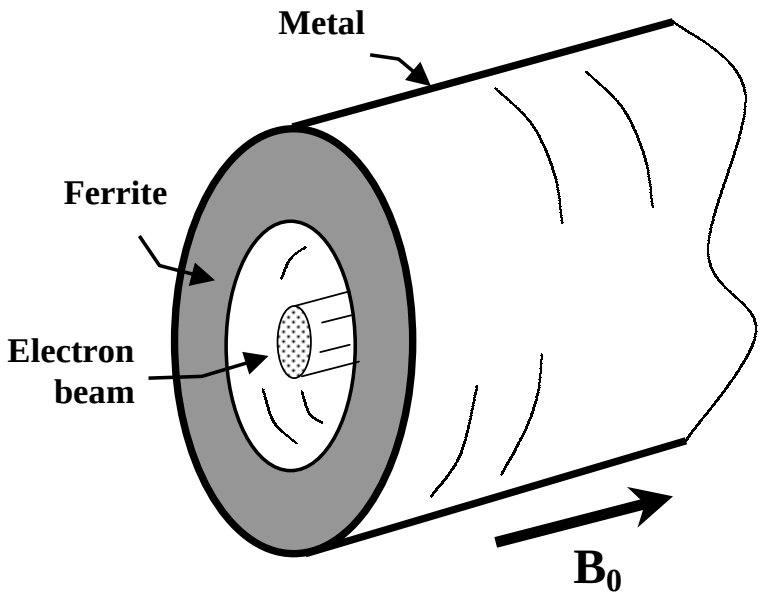

Figure 5.1: The proposed ferrite-guided CRM schemes in a cylindrical waveguide.

in this chapter shows that the ferrite loading may enable a new tunability feature of the CRM interaction since the waveguide spectral response is tuned simultaneously with the CRM interaction by the static magnetic field.

Ferrite-guided CRM's can be conceived in a variety of different schemes. In this chapter we study a cylindrical metallic waveguide loaded by a hollow ferrite rod as shown in Fig. 5.1 (other structures based on rectangular or planar waveguides are feasible as well). In the scheme shown in Fig. 5.1, an axial magnetic field is applied externally to activate both the CRM interaction and the ferrite unisotropic permeability.

Ferrite materials are widely used in a wide range of passive non-reciprocal

microwave devices, such as isolators, gyrators, circulators, filters, and phase shifters [71, 72]. Hence, these functions can be incorporated as well in future CRM schemes. For instance, one may conceive an "isolator-CRM" in which the backward waves or other spurious oscillations are suppressed selectively by the ferrite. The amplified forward-wave will not be attenuated then as in [10], since the resonance frequencies of the ferrite loss and of the forward CRM interaction deviate by the Doppler shift. Ferrite elements can be conceived also for phase shifting within the CRM interaction, to enhance its gain and efficiency.

This chapter is organized as follows. Section 5.2 presents a transverse-mode analysis for the cylindrical ferrite-loaded waveguide shown in Fig. 5.1, and a linear gain-dispersion relation of the corresponding CRM interaction. Section 5.3 introduces the extended tunability feature of a ferrite-loaded CRM. The discussion summarizes this chapter and proposes directions for future ferrite-guided CRM and CRM-array studies. The study in this chapter is published in Ref. [73].

5.2 Linear model

The linear model derived in this section demonstrates physical features of the ferrite-guided CRM. This model assumes an electron beam spiraling in a

Table 5.1: Parameters for numerical calculations

Parameter	**Symbol**	**Value**
Ferrite loaded cylindrical waveguide:		
Length	L	1 m
Ferrite inner/outer radius	R_i/R_o	5/8 mm
Relative dielectric factor	ε_r	12.9
Maximum magnetization	$4\pi\mu_0 M_i$	3 kG
Electron beam:		
Current	I	1 A
Voltage	V_{eb}	6–9 kV
Beam radius	r_b	2 mm
Pitch ratio	α	1

uniform magnetic field along a hole in the cylindrical ferrite-loaded waveguide illustrated in Fig. 5.1. This model presents the new features of this novel device, and it can be generalized to other schemes as well. The *em* wave propagating in the z-axis along with the electron beam is tuned to the range of a single circularly-polarized waveguide mode. Section 5.2.1 analyzes the transverse effects of the bounded ferrite medium on the guided *em*-wave. This

results in the mode dispersion and impedance, and the e-beam filling-factor parameters. These constitutive parameters are incorporated in Section 5.2.2 in the kinetic linear model derived for the convective cyclotron instability. This approach enables us to focus first on the principle attribution of the newly proposed ferrite guide to the CRM interaction.

In view of the CRM scheme shown in Fig. 5.1, we obtain from Maxwell's equations a tensor wave equation as follows

$$\nabla^2\mathbf{H} + \omega^2\varepsilon\underline{\underline{\mu}}\mathbf{H} = \begin{cases} -\nabla\times\mathbf{J} & 0 < r < r_b \\ \\ 0 & r_b < r < R_o \end{cases}, \tag{5.1}$$

where $\mathbf{H}$ is the magnetic field component of the *em* wave, ε is the (nonuniform) effective dielectric permitivity of the medium, ω is the *em* wave angular frequency, $\mathbf{J}$ and r_b are the electron-beam current and radius, respectively (assuming a pencil e-beam), and R_o is the inner radius of the metallic waveguide. The permeability tensor is given for the ferrite medium by [71] as:

$$\underline{\underline{\mu}} = \mu_0 \begin{pmatrix} \mu_r & -j\kappa_r & 0 \\ j\kappa_r & \mu_r & 0 \\ 0 & 0 & 1 \end{pmatrix}, \tag{5.2}$$

where the scalar permeability terms, neglecting losses, are:

$$\mu_r = 1 - \frac{\omega_0\omega_M}{\omega^2 - \omega_0^2}, \qquad \kappa_r = \frac{\omega\omega_M}{\omega^2 - \omega_0^2}. \tag{5.3a,b}$$

In vacuum, the permeability tensor $\underline{\underline{\mu}}$ is reduced to μ_0. The ferrite resonance and the magnetization angular frequencies are given by

$$\omega_0 = \frac{e}{m_0}\mu_0 H_i, \qquad \omega_M = \frac{e}{m_0}\mu_0 M_i \tag{5.4a,b}$$

respectively, both resemble the cyclotron angular frequency in the magnetized electron beam

$$\omega_{c0} = \frac{e}{m_0} B_0, \tag{5.5}$$

where e and m_0 are the electron charge and rest mass, respectively, H_i is the static magnetic induction inside the ferrite and M_i is its magnetization, and B_0 is the static magnetic field induced on the electron beam. The *em*-wave modes propagating in a magnetized ferrite medium are, inherently, circularly polarized waves [71, 72]. Their relative permeability, $\mu_{r\pm} = \mu_r \pm \kappa_r$, depends on frequency. The effect of the metallic bound is elaborated in the next section.

5.2.1 The ferrite-loaded cylindrical waveguide

The modes of *em*-wave propagation in a cylindrical waveguide partially filled with a ferrite tube (without an electron beam) were investigated by Baden-Fuller [74]. In this study he derived a comprehensive model for the dispersion relation and the transverse profiles of these waveguide modes. In this model, the homogeneous tensor wave-equation (Eq. (5.1) with $\mathbf{J} = 0$) for the

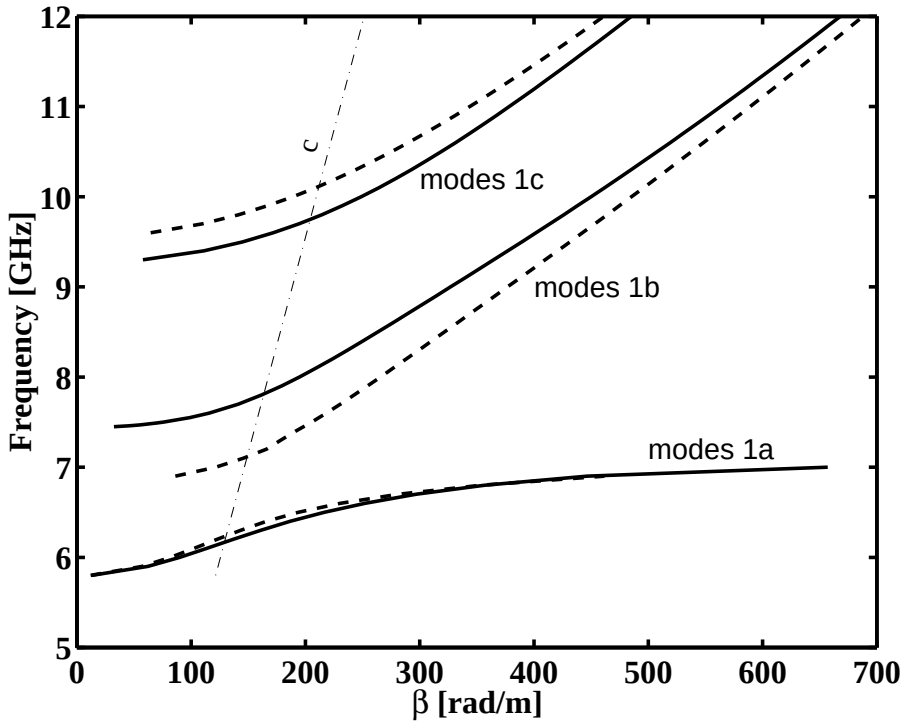

Figure 5.2: A computed dispersion relations of the first three modes in a ferrite-loaded cylindrical waveguide. The waveguide parameters are listed in Table 5.1. The external magnetization field of $B_0 = 2.5$ kG. The solid and dashed lines describe the right-hand (R) and left-hand (L) circular polarization modes, respectively. The free-space slope of c is also shown for comparison.

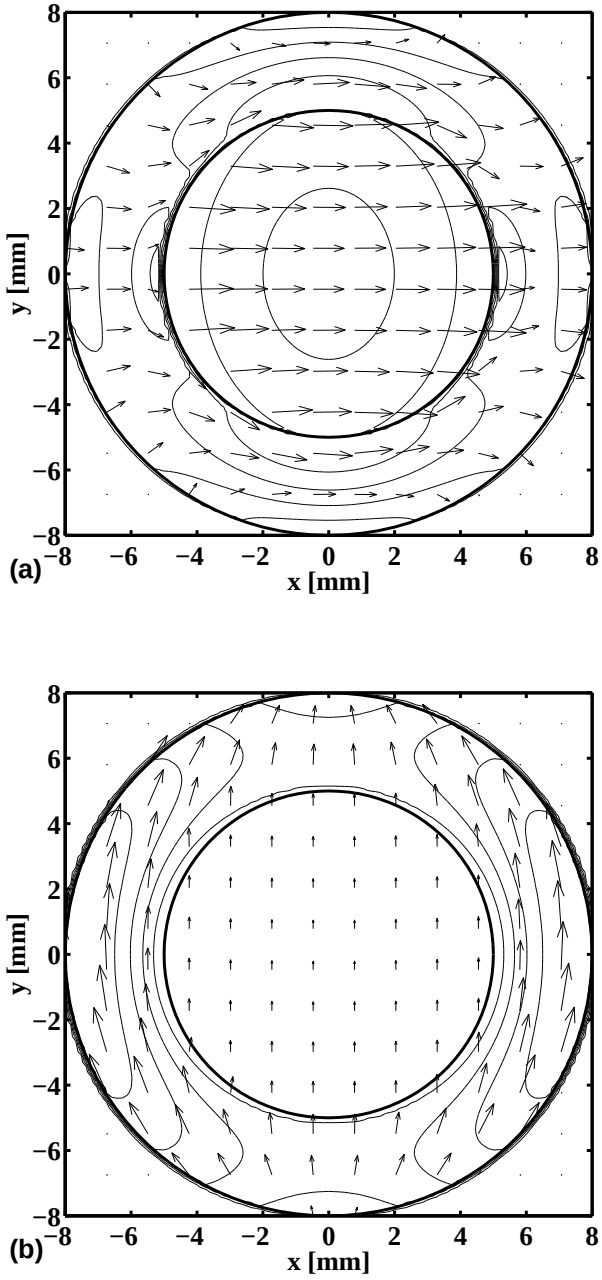

Figure 5.3: Computed transverse profiles of the electric (a) and magnetic (b) vector fields, respectively, and their corresponding intensity contours, across the partially filled ferrite loaded waveguide (without an e-beam), for the right-hand circularly polarized mode denoted "1b" in Fig. 5.2 at a frequency of 9 GHz, and B_0=2.5 kG.

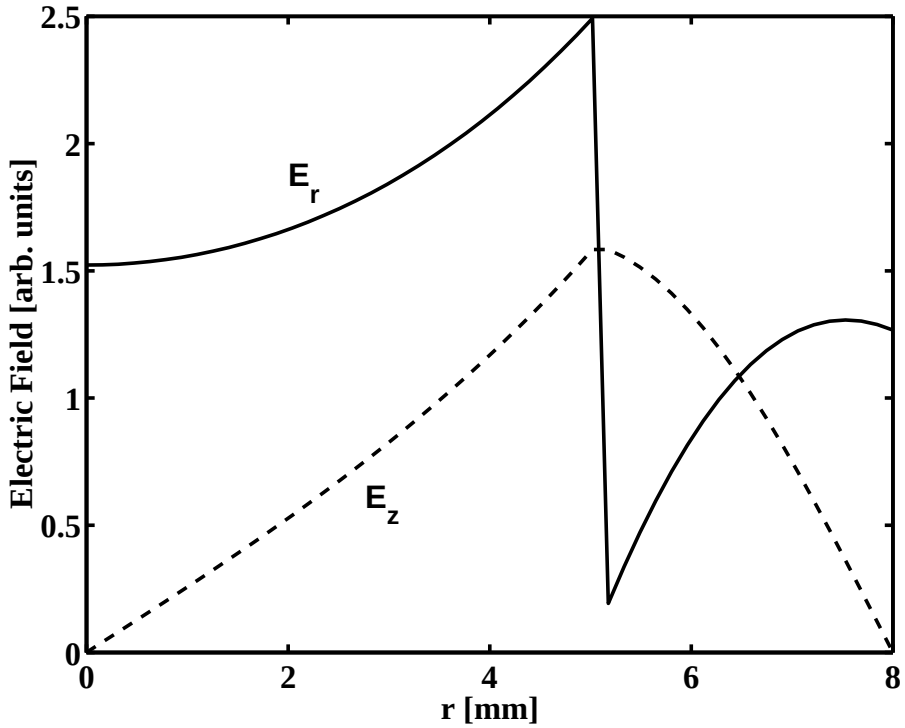

Figure 5.4: The magnitude of the radial and axial electric field components $|E_r(r)|$ (solid line) and $|E_z(r)|$ (dashed line), respectively, of Fig. 5.3 along its horizontal axis.

waveguide shown in Fig. 5.1 is leading to the coupled wave equation for the transverse and axial wave components, as follows

$$\mu_r \nabla_\perp^2 H_z + (\omega^2 \varepsilon \mu_0 \mu_r - \beta^2) H_z = j\omega\varepsilon\beta\kappa_r E_z \tag{5.6a}$$

$$\mu_r \nabla_\perp^2 E_z + [\omega^2 \varepsilon \mu_0 (\mu_r^2 - \kappa_r^2) - \mu_r \beta^2] E_z = -j\omega\mu_0\beta\kappa_r H_z, \tag{5.6b}$$

where β is the longitudinal wavenumber, and E_z and H_z are the longitudinal electric and magnetic field components. The ferrite-loaded cylindrical

waveguide supports composite *em* wave modes, which can not be classified as pure TE or TM modes as the empty waveguide modes. Hence, these modes posses both longitudinal E_z and H_z components due to the non-isotropic ferrite properties represented by the κ_r term in Eqs. (5.2) and (5.6a,b).

The waveguide modes are found in Ref. [74] by a sixth-order matrix dispersion equation of the form $\underline{\underline{\mathbf{D}}}(\beta)\underline{\mathbf{L}} = 0$ obtained by applying boundary conditions on the general solution of Eqs. (5.6a,b) on the inner and outer ferrite jacket surfaces. The β-dependent terms of the sixth-order matrix $\underline{\underline{\mathbf{D}}}$ are listed in [74]. The solution of the vector $\underline{\mathbf{L}}$ provides the coefficients for the *em*-wave components in the vacuum and ferrite media, as calculated below. The dispersion relation $\beta(\omega)$ of the ferrite-loaded waveguide modes is found by the numerical solutions of $\det \underline{\underline{\mathbf{D}}}(\beta) = 0$. Fig. 5.2 shows the computed dispersion relations for the left- and right-hand circularly polarized mode of the first three modes for the parameters listed in Table 5.1.

Ref. [74] presents general expressions for the various field components. These include the transverse magnetic field components in the waveguide bore region (i.e. the e-beam vicinity on axis) as follows

$$H_r = Z_0^{-1}[\frac{2\pi}{\gamma_a^2}\frac{n}{\bar{r}}K_3 J_n(\gamma_a \bar{r}) - \bar{\beta}\frac{2\pi}{\gamma_a}K_4 J_n'(\gamma_a \bar{r})]e^{j(n\theta+\omega t-\beta z)} \tag{5.7a}$$

$$H_\theta = jZ_0^{-1}[-\frac{2\pi}{\gamma_a^2}\bar{\beta}\frac{n}{\bar{r}}K_4 J_n(\gamma_a \bar{r}) + \frac{2\pi}{\gamma_a}K_3 J_n'(\gamma_a \bar{r})]e^{j(n\theta+\omega t-\beta z)}, \tag{5.7b}$$

where $Z_0 = \sqrt{\mu_0/\varepsilon_0}$ is the free-space wave impedance, K_3 and K_4 are coeffi-

cients resulted numerically from the vector $\underline{\mathbf{L}}$ solution, $\bar{r} = r/\lambda_0$ and $\bar{\beta} = \beta/k_0$ are the radial coordinate and the axial wavenumber, respectively (normalized to the free-space wavelength and wavenumber), $\gamma_a = 2\pi\sqrt{1-\bar{\beta}^2}$, and n is the azimuthal index of the mode. Unlike in uniform waveguides, discrete radial indices are not valid for the partially-filled ferrite waveguide. The mode presented by Eqs. (5.7a,b) is inherently circularly polarized.

The *em* wave profiles and the dispersion relations for the fundamental mode ($n = 1$) are computed here by the Baden-Fuller's model [74] for the parameters listed in Table 5.1. Fig. 5.3 presents the resulting profiles of the transverse *em* wave components across the partially filled cylindrical ferrite waveguide for the right-hand circularly polarized mode (at $B_0 = 2.5$ kG, $\omega/2\pi = 9$ GHz). Fig. 5.4 shows the magnitude of the radial and axial electric field components ($|E_r(r)|$ and $|E_z(r)|$, respectively) along the horizontal axis of Fig. 5.3. The computed results show that near the waveguide axis, the fundamental mode is dominated by the transverse field components. The wave profile is nearly uniform within the e-beam cross-section ($r \leq r_b$), and it can be regarded there as a quasi plane-wave. This circularly polarized quasi plane-wave can be characterized near axis by its local impedance Z_a and wavenumber β. In the conditions of Fig. 5.3, these are found to be $Z_a = 446\ \Omega$ and $\beta = 327\ \mathrm{m}^{-1}$, respectively.

For a single-mode CRM interaction, the transverse effect of the waveguide

is characterized also by the filling factor F_f which relates the effective cross-section areas of the e-beam and the em-mode as

$$F_f = \frac{A_{eb}}{A_{EM}} \tag{5.8}$$

where $A_{eb} = \int_{\theta=0}^{2\pi} \int_{r=0}^{r_b} (\underline{\mathbf{S}} \cdot \hat{\mathbf{z}}) r \, dr \, d\theta$ and $A_{EM} = \int_{\theta=0}^{2\pi} \int_{r=0}^{R_o} (\underline{\mathbf{S}} \cdot \hat{\mathbf{z}}) r \, dr \, d\theta$, and $\underline{\mathbf{S}} = \mathbf{E} \times \mathbf{H}^*$ is the Poynting vector of the *em* mode. The filling-factor, impedance, and wavenumber of the em-mode found above enable the derivation of the single-mode model for the ferrite-guided CRM interaction in the next section.

5.2.2 The cyclotron interaction

A linear model for the CRM interaction with a single waveguide mode is derived using the mode characteristics found above (i.e. the wave impedance, wavenumber, and filling factor parameters). Following Ref. [36], the electron current density is computed in the linear regime by

$$\mathbf{J} = -\frac{e}{m_0} \iiint_{\mathbf{P}_0} \frac{\mathbf{P}_c}{\gamma_0} f_{1c}(\mathbf{P}_0, z, \omega) \, d^3\mathbf{P}_0, \tag{5.9}$$

where $f_{1c}(\mathbf{P}_0, z, \omega)$ is the electron first-order distribution function, and $\mathbf{P}_c(\mathbf{P}_0)$ is the momentum characteristic line of the zero-order Vlasov equation. This line describes an electron spiraling trajectory along the axial magnetic field $\mathbf{B}_0 = \hat{\mathbf{z}} B_0$, as

$$\mathbf{P}_c = \hat{\mathbf{x}} P_{0\perp} \cos\psi(z) + \hat{\mathbf{y}} P_{0\perp} \sin\psi(z) + \hat{\mathbf{z}} P_{0z}, \tag{5.10}$$

where $\psi(z) = k_c z + \psi_0$ is the phase of the electron gyro-motion. The initial value of the momentum characteristic line is given in cylindrical coordinates by the initial components of the axial and radial electron momentum, P_{0z} and $P_{0\perp}$, respectively, and by the tilt angle α and the initial phase of the electron gyro-motion ψ_0. These are related to the Cartesian initial momentum components (P_{0x}, P_{0y}, P_{0z}) by $P_{0\perp} = \sqrt{P_{0x}^2 + P_{0y}^2}$, and $\alpha = \arctan(P_{0\perp}/P_{0z})$, where both Cartesian and cylindrical coordinates systems are used simultaneously in the following analysis. The relativistic factor in Eq. (5.9) is given by $\gamma_0 = \sqrt{1 + (P_{0z}^2 + P_{0\perp}^2)/m_0^2 c^2}$ where c is the speed of light. The cyclotron motion periodicity in Eq. (5.10) is given by $k_c = \omega_c / V_{0z}$, where $V_{0z} = P_{0z}/\gamma_0 m_0$ is the initial axial velocity of the electron. The relativistic cyclotron frequency is $\omega_c = \omega_{c0}/\gamma_0$.

The first-order distribution function $f_{1c}(\mathbf{P}_0, z, \omega)$ in Eq. (5.9) is the solution of the first-order Vlasov equation integrated along the zero-order characteristic lines (5.10), as follows:

$$j\omega f_{1c}(\mathbf{P}_0, z, \omega) + \frac{P_{0z}}{\gamma_0 m_0} \frac{\partial}{\partial z} f_{1c} + \mathbf{F}_{1c} \cdot \nabla_{p0} f_{0c}(\mathbf{P}_0) = 0 \qquad (5.11)$$

where $f_{0c}(\mathbf{P}_0)$ is the electron zero-order distribution function at the entrance to the interaction region ($z = 0$). The first-order force induced by the transverse *em* fields along the characteristic lines is given by

$$\mathbf{F}_{1c} = -e \left(\mathbf{E}_\perp + \frac{P_{cz}\mu_0}{\gamma_0 m_0} \hat{\mathbf{z}} \times \mathbf{H}_\perp + \frac{\mu_0}{\gamma_0 m_0} \mathbf{P}_{c\perp} \times \mathbf{H}_\perp + \hat{\mathbf{z}} E_z \right). \qquad (5.12)$$

For a CRM interaction with a single circularly polarized wave, we assume a slowly varying wave amplitude $A(z)$ along the interaction region. The *em* wave propagating in the ferrite-loaded waveguide, in the region of the electron beam, is described by the transverse components of the wave equation (5.1) as

$$\mathbf{H}_\perp = \pm j A(z)\hat{\mathbf{e}}^\pm \hat{\phi}_H^\pm H_0\, e^{-j\beta z}, \tag{5.13a}$$

$$\mathbf{E}_\perp = A(z)\hat{\mathbf{e}}^\pm \hat{\phi}_E^\pm H_0 Z_a^\pm e^{-j\beta z}, \tag{5.13b}$$

and by the axial component of the electric field $E_z = A(z)\hat{\phi}_{Ez}^\pm E_{z0}\, e^{-j\beta z}$, where $+/-$ denote a right/left hand polarization, and $\hat{\mathbf{e}}^\pm = \hat{\mathbf{x}} \mp j\hat{\mathbf{y}}$ is the circularly polarized unit-vector. The transverse profiles of the *em* mode are $\hat{\phi}_H^\pm$, $\hat{\phi}_E^\pm$, and $\hat{\phi}_{Ez}^\pm$ (note that within the e-beam cross-section $\hat{\phi}_H^\pm \approx \hat{\phi}_E^\pm$). The initial transverse magnetic-field is H_0, and E_{z0} is the initial axial electric-field. The longitudinal wavenumber β is found as described in Section 5.2.1 above.

Assuming a uniform initial azimuthal distribution of the electron beam, the distribution function $f_{0c}(\mathbf{P}_0)$ is independent of ψ_0. Consequently, $\partial f_{0c}/\partial P_{0x} = (\partial f_{0c}/\partial P_{0\perp})\cos\psi$, $\partial f_{0c}/\partial P_{0y} = (\partial f_{0c}/\partial P_{0\perp})\sin\psi$, and the Vlasov equation

(5.11) is rewritten in the form

$$j\omega f_{1c}(\mathbf{P}_0, z, \omega) + \frac{P_{0z}}{\gamma_0 m_0}\frac{\partial}{\partial z} f_{1c} = e\left[\left(Z_a^{\pm} - \frac{P_{0z}\mu_0}{\gamma_0 m_0}\right)\frac{\partial f_{0c}}{\partial P_{0\perp}} + \frac{P_{0\perp}\mu_0}{\gamma_0 m_0}\frac{\partial f_{0c}}{\partial P_{0z}}\right] A(z)\hat{\phi}_H^{\pm} H_0\, e^{-j(\beta z \pm k_c z \pm \psi_0)} + e\frac{\partial f_{0c}}{\partial P_{0z}} A(z)\hat{\phi}_{Ez}^{\pm} E_{z0}\, e^{-j\beta z}. \quad (5.14)$$

Substituting Eq. (5.13) into the wave equation (5.1), subtracting the homogeneous components (which does not include derivatives of $A(z)$ and therefore equal to zero), and neglecting second derivatives of $A(z)$, yield the wave equation for the e-beam region ($r < r_b$)

$$\pm 2\beta \frac{dA(z)}{dz}\,\hat{\mathbf{e}}^{\pm}\hat{\phi}_H^{\pm} H_0\, e^{-j\beta z} = -\frac{\partial}{\partial z}(\hat{\mathbf{z}} \times \mathbf{J}_\perp) + \hat{\mathbf{z}} \times \nabla_\perp J_z. \quad (5.15)$$

Equations (5.9), (5.14), and (5.15) form a linear set of partial differential equations. In order to solve them, we apply Laplace transform on the z dimension, $\tilde{A}(s) = \int_z A(z)e^{-sz}dz$, and rewrite Eqs. (5.9), (5.14), and (5.15) in the s domain as follows. The current components (5.9) are transformed to

$$\tilde{\mathbf{J}}_\perp(s,\omega) = -\frac{e}{2m_0}\iiint_{\mathbf{P}_0} \frac{P_{0\perp}}{\gamma_0}\left[e^{j\psi_0}\tilde{f}_{1c}(s - jk_c)\hat{\mathbf{e}}^{+} + e^{-j\psi_0}\tilde{f}_{1c}(s + jk_c)\hat{\mathbf{e}}^{-}\right] d^3\mathbf{P}_0 \quad (5.16a)$$

and

$$\tilde{J}_z(s,\omega) = -\frac{e}{m_0}\iiint_{\mathbf{P}_0} \frac{P_{0z}}{\gamma_0}\tilde{f}_{1c}(s)\, d^3\mathbf{P}_0, \quad (5.16b)$$

where the first-order distribution function is given by the solution of the transformed first-order Vlasov equation (5.14) as follows:

$$\tilde{f}_{1c}(\mathbf{P}_0, s, \omega) = e\left(j\omega + \frac{P_{0z}}{\gamma_0 m_0}s\right)^{-1}\Big\{\left[\left(Z_a^{\pm} - \frac{P_{0z}\mu_0}{\gamma_0 m_0}\right)\frac{\partial f_{0c}}{\partial P_{0\perp}} + \frac{P_{0\perp}\mu_0}{\gamma_0 m_0}\frac{\partial f_{0c}}{\partial P_{0z}}\right]\cdot \tilde{A}(s+j\beta \pm jk_c)e^{\mp j\psi_0}\hat{\phi}_H^{\pm}H_0 + \frac{\partial f_{0c}}{\partial P_{0z}}\tilde{A}(s+j\beta)\hat{\phi}_{Ez}^{\pm}E_{z0}\Big\}. \quad (5.17)$$

The wave equation (5.15) is transformed to

$$\pm 2\beta\left[(s+j\beta)\tilde{A}(s+j\beta) - A_0\right]\hat{\mathbf{e}}^{\pm}\hat{\phi}_H^{\pm}H_0 = -s\left(\hat{\mathbf{z}}\times\tilde{\mathbf{J}}_{\perp}(s,\omega)\right) + \hat{\mathbf{z}}\times\nabla_{\perp}\tilde{J}_z(s,\omega), \quad (5.18)$$

where A_0 is the wave amplitude at the entrance ($z = 0$).

Substituting the distribution function (5.17) into the current components (5.16a,b) yields the expressions

$$\tilde{\mathbf{J}}_{\perp}^{\pm}(s,\omega) \cong -\frac{\pi e^2}{m_0}\tilde{A}(s+j\beta)\hat{\mathbf{e}}^{\pm}\hat{\phi}_H^{\pm}H_0\int_{P_{0z}}\int_{P_{0\perp}}\frac{P_{0\perp}}{\gamma_0}\left(j\omega + \frac{P_{0z}}{\gamma_0 m_0}s \mp \frac{j\omega_{c0}}{\gamma_0}\right)^{-1}\cdot \left[\left(Z_a^{\pm} - \frac{P_{0z}\mu_0}{\gamma_0 m_0}\right)\frac{\partial f_{0c}}{\partial P_{0\perp}} + \frac{P_{0\perp}\mu_0}{\gamma_0 m_0}\frac{\partial f_{0c}}{\partial P_{0z}}\right]P_{0\perp}\,dP_{0\perp}\,dP_{0z}, \quad (5.19a)$$

and

$$\tilde{J}_z^{\pm}(s,\omega) \cong -\frac{2\pi e^2}{m_0}\tilde{A}(s+j\beta)\hat{\phi}_{Ez}^{\pm}E_{z0}\int_{P_{0z}}\int_{P_{0\perp}}\frac{P_{0z}}{\gamma_0}\left(j\omega + \frac{P_{0z}}{\gamma_0 m_0}s\right)^{-1}\cdot \frac{\partial f_{0c}}{\partial P_{0z}}P_{0\perp}\,dP_{0\perp}\,dP_{0z}, \quad (5.19b)$$

where terms independent of ψ_0 are vanished by the integration.

We assume now that the dominant poles are located in the s plane in the vicinity of the cyclotron-resonance condition, hence

$$\left| j\omega + \frac{P_{0z}}{\gamma_0 m_0} s \mp \frac{j\omega_{c0}}{\gamma_0} \right| \sim 0, \tag{5.20}$$

where the $-/+$ signs correspond to the normal and anomalous modes of the CRM interaction, respectively. Side-band harmonics and other off-resonance effects which do not satisfy (5.20) are negligible. In particular, the axial current $\tilde{J}_z$ (5.19b), associated with the traveling-wave tube (TWT) or Cerenkov axial bunching effect, is off-resonance in the CRM resonance condition (5.20) and therefore negligible (note that $V_{0z} \approx (\omega - \omega_c)/\beta$ is much smaller than the *em* phase velocity $V_{ph} = \omega/\beta$, thus the denominator of (5.19b) exceeds the order of ω_c). Therefore, even if $|E_z| \lesssim |\mathbf{E}_\perp|$ the effect of J_z is negligible with respect to $\mathbf{J}_\perp$ near the cyclotron resonance.

After integration by parts and some further algebraic steps, Eq. (5.19a) results in

$$\tilde{\mathbf{J}}_\perp^\pm(s,\omega) \cong \tilde{A}(s+j\beta)\hat{\mathbf{e}}^\pm \hat{\phi}_H^\pm H_0 \frac{2\pi e^2}{m_0} \int_{P_{0z}} \int_{P_{0\perp}} \frac{1}{\gamma_0} \left[\left(j\omega + \frac{P_{0z}}{\gamma_0 m_0} s \mp \frac{j\omega_{c0}}{\gamma_0} \right)^{-1} \cdot \left(Z_a^\pm - \frac{P_{0z}\mu_0}{\gamma_0 m_0} \right) - \frac{1}{2} \left(j\omega + \frac{P_{0z}}{\gamma_0 m_0} s \mp \frac{j\omega_{c0}}{\gamma_0} \right)^{-2} \left(\frac{P_{0\perp}}{\gamma_0 m_0} \right)^2 \left(\frac{j\omega}{c^2} Z_a^\pm + s\mu_0 \right) \right] \cdot f_{0c} P_{0\perp}\, dP_{0\perp}\, dP_{0z}. \tag{5.21}$$

In the ideal case of a cold and azimuthaly uniform electron beam, the zero-

order electron distribution on-axis is approximated by

$$f_{0c}(\mathbf{P}_0) \cong \frac{n_0}{2\pi \bar{P}_{0\perp}} \delta(P_{0\perp} - \bar{P}_{0\perp}) \delta(P_{0z} - \bar{P}_{0z}), \tag{5.22}$$

where n_0 is the electron density and δ is a Dirac function. We substitute the current equation (5.21) in the ideal limit (5.22) into the wave equation (5.18). In the region of the electron beam $Z_a^{\pm} = V_{ph}^{\pm}\mu_0$, where $V_{ph}^{\pm}$ is the *em* phase-velocity of the homogeneous solution. The above results in

$$\begin{aligned} -2j\beta \left[(s+j\beta)\tilde{A}(s+j\beta) - A_0\right] = \frac{\omega_p^2}{c^2} F_f \left[\frac{s}{j(\omega \mp \omega_c) + s\bar{V}_{0z}}(V_{ph}^{\pm} - \bar{V}_{0z})\right. \\ \left. -\frac{\bar{V}_{0\perp}^2}{2} \frac{s}{[j(\omega \mp \omega_c) + s\bar{V}_{0z}]^2} \left(\frac{j\omega}{c^2} V_{ph}^{\pm} + s\right)\right] \tilde{A}(s+j\beta), \end{aligned} \tag{5.23}$$

where $\omega_p = \sqrt{e^2 n_0 / \gamma_0 m_0 \varepsilon_0}$ is the plasma angular frequency, F_f is the e-beam filling factor (5.8) for the fundamental *em*-mode, and $\bar{V}_{0z} = \bar{P}_{0z}/\gamma_0 m_0$ and $\bar{V}_{0\perp} = \bar{P}_{0\perp}/\gamma_0 m_0$ are the average electron axial and perpendicular velocity components, respectively. This yields

$$\begin{aligned} -2j\beta \left[s\tilde{A}(s) - A_0\right] = \frac{1}{c}\omega_p^2 F_f \frac{s - j\beta}{j(\omega \mp \omega_c) + (s - j\beta)\bar{V}_{0z}} \\ \cdot \left[(\bar{\beta}_{ph}^{\pm} - \bar{\beta}_{0z}) - \frac{1}{2}\bar{\beta}_{0\perp}^2 \frac{j\omega\bar{\beta}_{ph}^{\pm} + (s - j\beta)c}{j(\omega \mp \omega_c) + (s - j\beta)\bar{V}_{0z}}\right] \tilde{A}(s) \quad , \end{aligned} \tag{5.24}$$

where $\bar{\beta}_{0z} = \bar{V}_{0z}/c$, $\bar{\beta}_{0\perp} = \bar{V}_{0\perp}/c$, and $\bar{\beta}_{ph}^{\pm} = V_{ph}^{\pm}/c$ are the normalized electron and phase velocity components.

The dimensionless operating parameters of the ferrite-guided CRM inter-

action are defined as follows. The tuning parameter is

$$\hat{\theta}^{\mp} = (\omega \mp \omega_c - \beta \bar{V}_{0z}) \frac{L}{\bar{V}_{0z}} \tag{5.25}$$

where L is the interaction length. The normalized space-charge parameter is $\hat{\theta}_p = \omega_p L/\bar{V}_{0z}$, and the dimensionless wavenumber variables are $\hat{s} = jsL$, $\hat{k} = kL$ and $\hat{\beta} = \beta L$. This notation leads to a simplified gain-dispersion relation for the ferrite-guided CRM interaction as in Ref. [36]

$$\tilde{A}(\hat{s}) = \frac{(\hat{s} - \hat{\theta}^{\mp})^2}{\hat{s}(\hat{s} - \hat{\theta}^{\mp})^2 - \kappa(\hat{s}) F_f C(\hat{s}) \hat{\theta}_p^2} A_0. \tag{5.26}$$

where the coupling term for the circularly polarized wave in the ferrite-guided CRM is

$$\kappa(\hat{s}) = \bar{\beta}_{0z}(\hat{s} - \hat{\theta}^{\mp})(\bar{\beta}_{ph}^{\pm} - \bar{\beta}_{0z}) - \frac{1}{2}\bar{\beta}_{0\perp}^2(\hat{s} + \hat{\beta} - \hat{k}\bar{\beta}_{ph}^{\pm}), \tag{5.27}$$

and the ratio parameter $C(\hat{s}) = (\hat{s} + \hat{\beta})/2\hat{\beta}$ is close to $\frac{1}{2}$ for slow waves. The resulting Pierce-type equation (5.26) for the ferrite-guided CRM interaction with a single circularly polarized mode is solved for several representing cases to demonstrate the ferrite effect in the next section.

5.3 Ferrite-CRM tunability

The unique feature of the ferrite-loaded waveguide stems from the dependence of its dispersion relation on the induced external magnetic field. This

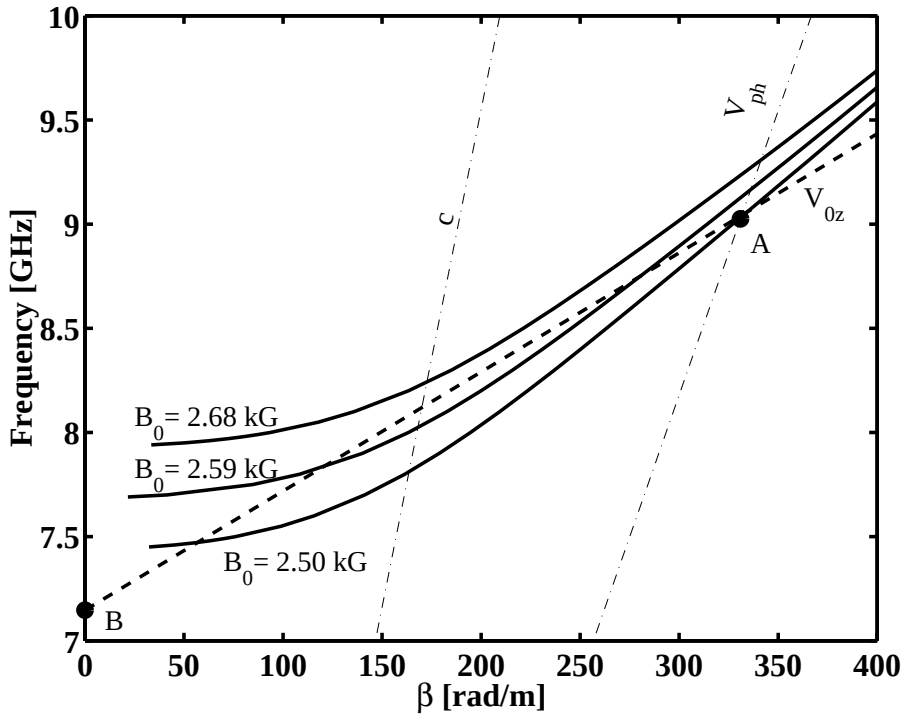

Figure 5.5: The dispersion relation of the right-hand circularly polarized mode denoted "1b" in Fig. 5.2 for three values of the external magnetic field, B_0 =2.50, 2.59, and 2.68 kG. The dashed line shows the electron beam line for the operating parameters of Table 5.1 with B_0=2.5 kG and V_{eb}=7.5 kV. The Points A and B denote the CRM interaction point and the cyclotron frequency, respectively. The dotted lines present the *em* phase velocity slope V_{ph} and the free-space slope c ($V_{0z} = 0.12c$ and $V_{ph} = 0.57c$).

effect is shown for instance in Fig. 5.5 for the parameters listed in Table 5.1. The dependence of the dispersion relation on the magnetic field enables to vary the waveguide mode cutoff-frequency, and to shift its entire dispersion curve according to the axial static magnetic field. Fig. 5.5 shows for instance the variation in the dispersion relation of the right-hand circularly polarized mode (denoted "1b" in Fig. 5.2) for three values of the external magnetic field (2.50, 2.59, and 2.68 kG). An increase of B_0 by 0.09 kG leads to an increase of 0.25 GHz in the ferrite resonance frequency, and consequently to a similar increase of the waveguide cut-off frequency. Hence, in the ferrite-loaded CRM, the frequency range can be tuned not only by varying the e-beam energy but also by the axial magnetic field effect on the ferrite. Here, the magnetic field affects not only the electron-cyclotron frequency (as in an ordinary CRM), but also the ferrite-resonance frequency and consequently the spectral response of the waveguide.

Fig. 5.5 shows for instance the e-beam line for B_0=2.5 kG, V_{eb}=7.5 kV, and the other parameters listed in Table 5.1. The CRM interaction with the corresponding *em* wave is denoted as Point A in this dispersion diagram. The phase velocity at this point is $0.57c$, whereas the electron axial velocity is $0.12c$, hence the two are intentionally mismatched ($V_{ph} \sim 5V_{0z}$).

The tunability feature of the ferrite-loaded CRM device is demonstrated in this section by a numerical example. The gain-dispersion relation (5.26)

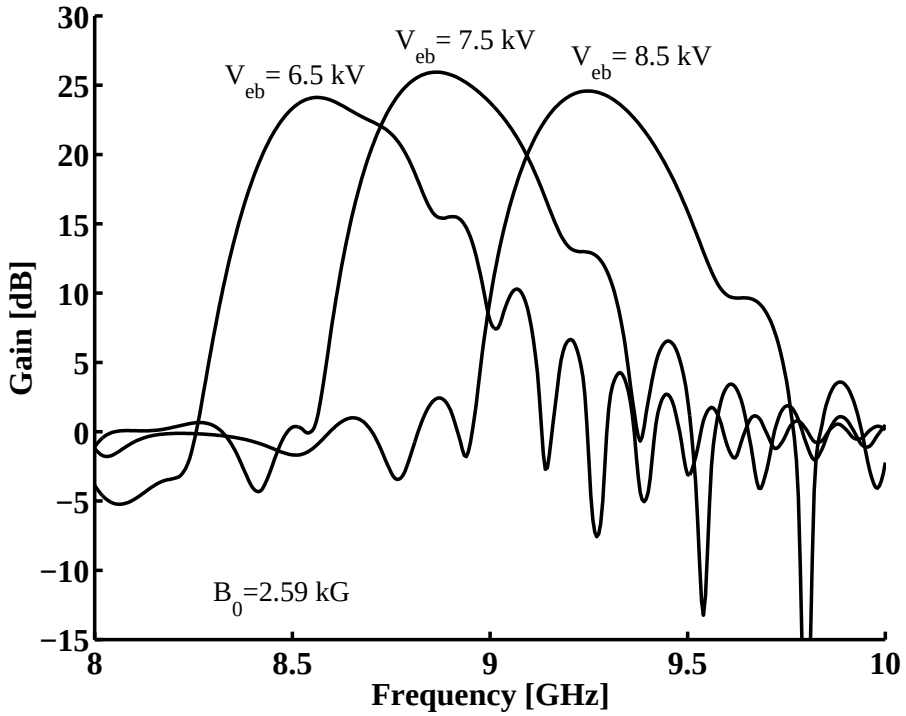

Figure 5.6: Gain vs. frequency for $B_0 = 2.59$ kG, and e-beam voltages of 6.5, 7.5, and 8.5 kV, for the parameters listed in Table 5.1.

is solved by an inverse Laplace transform of $\tilde{A}(\hat{s})$ for the parameters listed in Table 5.1. Fig. 5.6 shows gain curves of the CRM interaction in three different e-beam voltages (6.5, 7.5, and 8.5 kV) for the same static magnetic field (2.59 kG). This tuning effect, by varying the electron energy, is similar in principle to the ordinary CRM. But, in a ferrite-guided CRM a variation in the static magnetic field leads to a wider tunability range because of the ferrite response to this field. Fig. 5.7 demonstrates this feature by three gain curves of the CRM interaction in different magnetic fields (2.50, 2.59, and

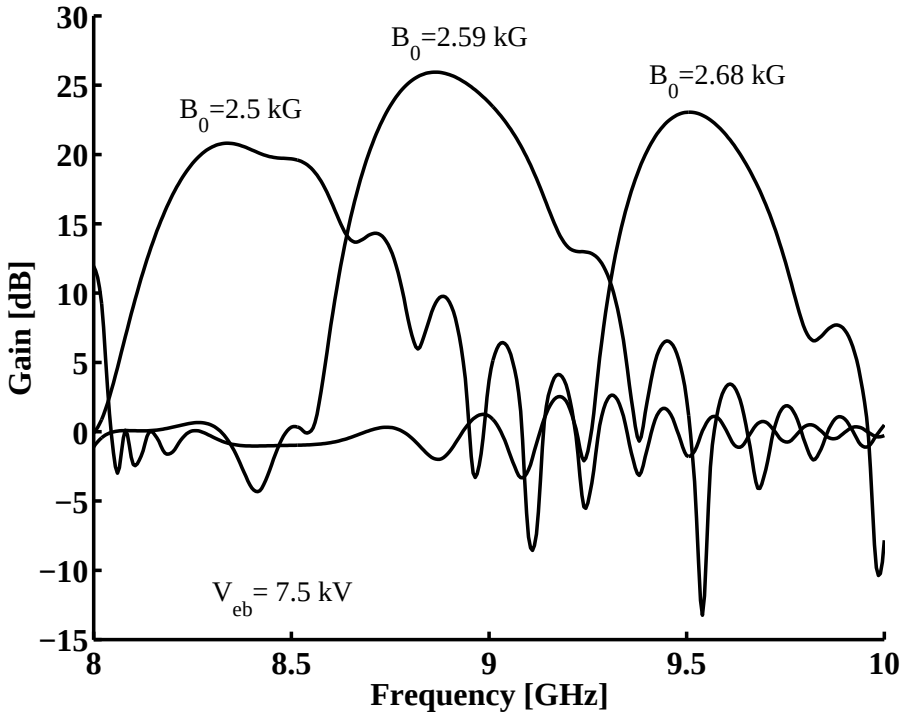

Figure 5.7: Gain vs. frequency for e-beam voltage of 7.5 kV, and external magnetic fields of 2.50, 2.59, and 2.68 kG, for the parameters listed in Table 5.1.

2.68 kG) for the same e-beam voltage (7.5 kV). The instantaneous bandwidth is ~ 0.3 GHz and the tunability range attains 1.2 GHz in this example.

It should be noted that this CRM performance in such a low operating voltage are not achievable in an empty waveguide of the same diameter (16 mm), because its cutoff frequency (11 GHz) is higher than that of the ferrite-loaded waveguide (7.5 GHz).

5.4 Discussion

The concept of ferrite-guided CRM is proposed and discussed theoretically in this chapter. The ferrite medium slows the *em* wave and enhances its magnetic field component. This enables a CRM interaction in the Weibel regime, in which the axial bunching mechanism is dominant. The ferrite-guided CRM may attain as well the anomalous Doppler condition (with the left-hand circular polarization modes).

A linear gain dispersion equation (5.26) is derived in this chapter using the formalism of Ref. [36], whereas the ferrite-loaded waveguide parameters (i.e. the wavenumber, phase velocity, impedance, and filling factor) are found numerically according to Ref. [74]. Unlike in an ordinary CRM, the waveguide parameters depend on the axial-magnetic field strength, which add another dimension of tunability to this CRM scheme. The gain vs. frequency of the ferrite-guided CRM amplifier is calculated numerically for several examples to demonstrate this tunability features.

The slow-wave interaction widens the spectral bandwidth of the amplification curve, but unlike dielectric-loaded CRM schemes, the spectral response of the ferrite-guide depends on the induced magnetic field, and it can be made selective in frequency. For instance, the losses associated with the ferrite resonance frequency (which differs from the CRM operating frequency

by the Doppler shift and therefore neglected in this study) can be utilized in future schemes to suppress selectively backward waves and other spurious oscillations. This may extend the concept demonstrated by Chu *et al.* [10] with a resistive load. In future schemes, ferrite components can be incorporated within CRM tubes as internal phase-shifters to enhance its gain and efficiency.

Ferrite-guided CRM's can be made in rectangular and planar shapes as well, and may be incorporated in coupled and uncoupled CRM-arrays. The ferrite-guiding in CRM-arrays may enable unique array features, such as the wide tunability, low-voltage operation, and to guide the *em* wave in a selective mode.

Chapter 6

Four Electron-Beam CRM Array

6.1 Introduction

In CRMs and gyrotron oscillators, the high-power microwave is extracted from the interaction with a single high-voltage high-current electron beam. However, high-voltage operation requires expensive power supplies and a special care to prevent voltage break-down, and results in a large system overhead [15]. High current operation is limited by the space-charge forces of the electron beam [16], and results in a wide cavity cross-section and a mode competition due to high mode operation [75, 76, 77].

The multi-beam CRM array concept was proposed by Jerby *et al.* [18, 19]

to alleviate these difficulties by increasing the CRM dimensionality. Namely, to increase the number of interaction channels rather than increasing the power of the single electron beam. Such approach can alleviate also other technological difficulties such as decreasing the mode-competition in an over-moded waveguide while distributing the output power over a large window aperture.

Microwave tube arrays can operate as active array antennas. A direction finder by traveling-wave-tube (TWT) active-array is described by Kummer [78]. Angular steering method by free-electron laser (FEL) array, proposed in Ref. [34], was demonstrated by Cecere and Marshall [37]. Lobe steering by an uncoupled CRM-array and the measurements of phase and gain of the CRM-element are described in Chapters 2 and 3, respectively.

Periodic structures can be used in CRMs for dielectric loading and for mode selectivity. A linear analysis of periodic-waveguide cyclotron maser interaction was presented in Ref. [36]. Such loading can enable a low-voltage operation as obtained in Refs. [64, 65]. A selective mode operation by a photonic band-gap gyrotron is presented by Sirigiri *et al.* [79].

Multi-beam related studies include the cluster klystron [80], the double-stream cyclotron maser interaction [81], and the multi-beam stagger-tuned gyroklystrons [82]. A linear analysis of a multi-beam CRM interaction in a periodic waveguide was carried in Ref. [24]. An experimental study of one-

and two-beam CRM interaction in a periodic waveguide was presented in Ref. [83]. The use of carbon-fiber cathodes in a multi-beam CRM device is described in Ref. [84].

In order to demonstrate the multi-beam effect in a coupled CRM-array oscillator, an experimental device with four symmetrically located electron beams has been studied experimentally. The objectives of this study are (a) to demonstrate a low-voltage low-current simultaneous interaction of four electron beams in a periodic waveguide, (b) to measure the output power for the interaction of each electron beam separately, and (c) to compare the results of the single and the simultaneous 4-beam interaction measurements.

6.2 Experimental setup

The multi-beam CRM experimental scheme is shown in Fig. 6.1(a). The experimental operating parameters are listed in Table 6.1. Four linear electron-beams are generated by an electron-gun array based on four thermionic cathodes (Heatwave STD200). A cylindrical plate with four 7 mm diameter through-holes is placed 5 mm from the cathode plane to serve as an anode array.

The beams are focused by a focusing coil into the kicker section. The kicker array consists on 4 magnet pairs. Each pair is located near its corre-

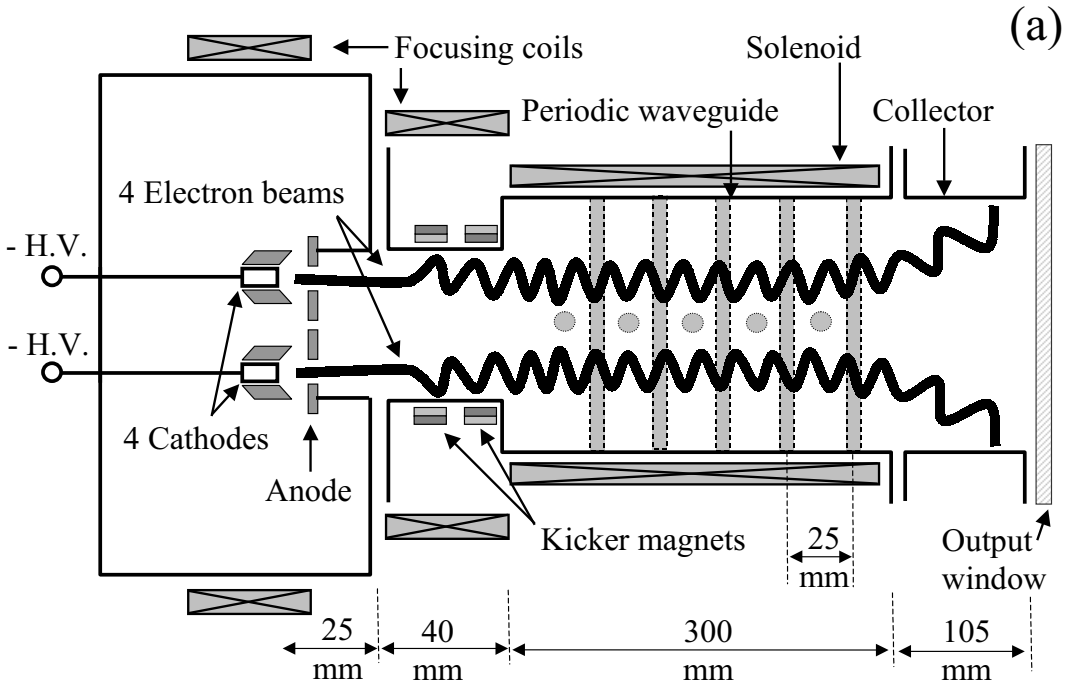

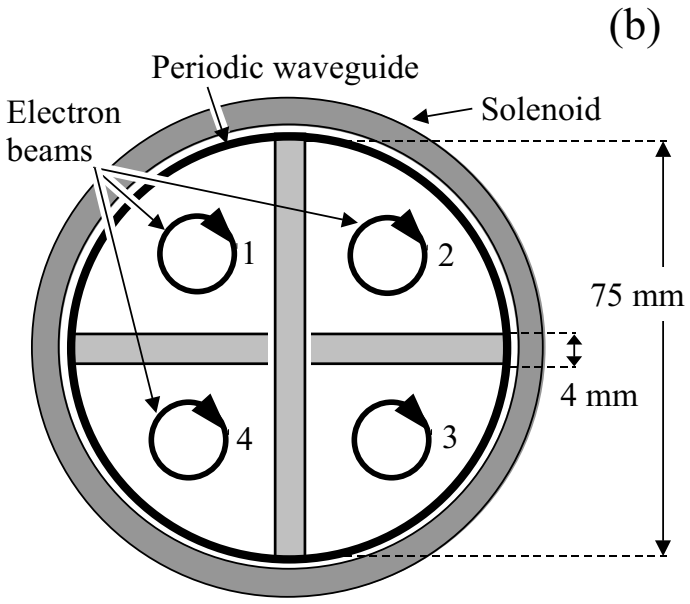

Figure 6.1: The multi-beam CRM experimental scheme (a), and its cross section in which the electron-beams are numbered from 1 to 4 (b).

Table 6.1: Experimental operating parameters

Number of electron beams	1–4	
Electron beam voltage	10–19	kV
Electron beam current	0.3–0.8	A
Kicker pitch-ratio	1	
Pitch-ratio spread	10–15	%
Solenoid magnetic field	~ 1.3	kG
Cyclotron harmonic number	1	
Waveguide diameter	75	mm
Waveguide length	30	cm
Post diameter	4	mm
Period length	25	mm
Number of periods	10.5	
Frequency pass-band	3.7–4.2	GHz

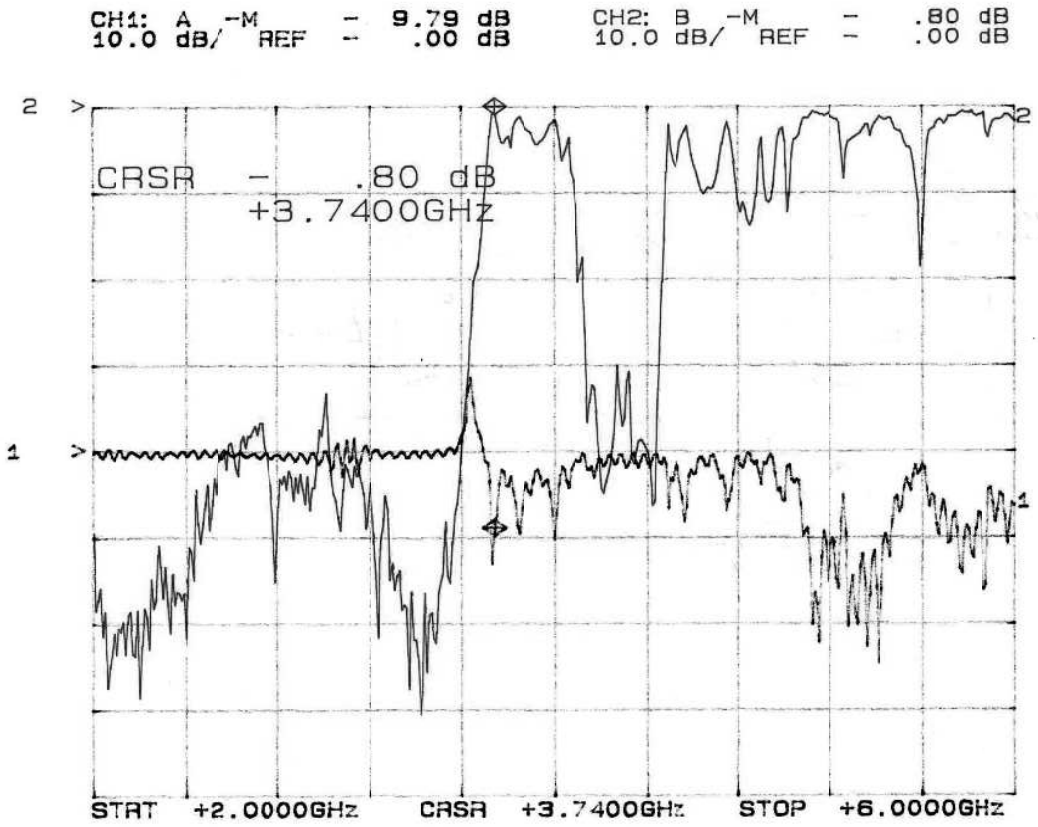

Figure 6.2: Periodic waveguide cold measurements by a scalar network analyzer (HP 8757A) . The reflection and transmission traces are shown in Channel 1 and 2, respectively.

sponding beam and consists of two plates of Neodymium Iron Boron (NdFeB) permanent magnets. The magnets are attached to the kicker pipe and are poled into and out of it in the transverse direction. This kicker configuration resembles a wiggler's half period. The electron gun is designed by the Herrmannsfeldt EGUN simulation code [44], and the kicker electron optics is optimized by a MATLAB program to provide a pitch-ratio of $\alpha = 1$ with

a spread of $\Delta\alpha/\alpha = 10\%$ [85].

The beams are rotating in the cyclotron frequency along the periodic waveguide as shown in Figs. 6.1(a,b). The axial magnetic field is produced by a 0.3 m long solenoid which is wrapped around the waveguide outer-wall. This configuration gives a $\sim$ 0.14 m interaction length in which the axial magnetic field is constant within a 1% margin. The 0.3 m periodic waveguide is succeeded by a 0.1 m non-periodic waveguide extension operating as a collector.

The electron-gun is fed by a 19 kV pulse generator. The solenoid and focusing coil are connected in series and fed by a current pulser. The maximal axial magnetic field is 1.6 kG, obtained in a pulse duration of $\sim$ 10 ms.

The periodic waveguide consist of a circular waveguide (diameter 75 mm) in which horizontal and vertical posts are located along its axis in consequent order. The distance between each two (horizontal and vertical) posts is 12.5 mm and the total number of posts is 21 (10.5 periods of posts).

Prior to installation, the periodic waveguide was connected through waveguide to coax adapters (RA187-SMA-F-1B-C) to a scalar network analyzer (HP 8757A) for cold measurements. The adapters' polarization was parallel to each other and to the vertical posts. The reflection (Channel 1) and transmission (Channel 2) traces are shown in Fig. 6.2. A clear pass-band between 3.7–4.2 GHz is seen in the transmission trace. This pass-band trace

is typical in periodic waveguide measurements [19].

The kicker pipe has an inner diameter of 47 mm, which corresponds to a fundamental TE_{11} cut-off frequency of 3.5 GHz. Since this cut-off frequency is lower than the periodic waveguide pass-band, backward-wave oscillations might be absorbed at the region of the multi-electron gun and the vacuum pump. For this reason, the experiment is operated with two configurations: (a) with a hollow kicker-pipe, and (b) with a reflector inside the kicker, by dividing the kicker pipe into four quarters with two metallic plates, combined transversely to each other.

In the first configuration the microwave output power is coupled from the output window by one waveguide to coax adapter (RA187-SMA-F-1B-C) into a microwave diagnostic setup for power and frequency measurements. The adapter is rotated 45° with respect to the metallic posts in order to couple out both horizontal and vertical TE modes. The power measurements consist of a dummy load and a crystal power detector (HP 423B). A sample of the output power is connected through a mixer (Magnum Microwave MM134P-1) into a frequency and time interval analyzer (HP 5372A) for frequency measurements. The mixer local signal is fed by a synthesized sweeper (HP 83752A).

In the second configuration, the microwave output power is coupled from the output window into the diagnostic setup by two antenna-probes, trans-

verse to each other and aligned with the vertical and horizontal metallic posts, respectively. The power measurements from each probe consist of a dummy load and a crystal power detector (ACTP-1502N). A sample of the output power from the vertical probe is coupled to the frequency and time interval analyzer, as described above. The power sum from the two probe outputs is calculated.

6.3 Experimental results

The multi-beam CRM oscillator described at the experimental setup section was operated with the parameters listed in Table 6.1, where no reflector was present inside the kicker pipe. Raw measurements of the electron-beam voltage and current are shown in Fig. 6.3. The current shown was measured on the collector. Its transmission with respect to the input current (not show) is $\sim 25\%$ for the electron-beam of cathode 1, and $\sim 70\%$ for electron beams 2,3, and 4. It is seen in Figs. 6.3(b) and (c) that the current increases proportionally to the number of operating cathodes, and a total current of 2.2 A is measured at a beam voltage of 18 kV.

An example for a raw measurement of the microwave output power vs. time is shown in Fig. 6.4. The power is presented for the condition of Fig. 6.3(c), when all four cathodes were operated. The maximum obtained

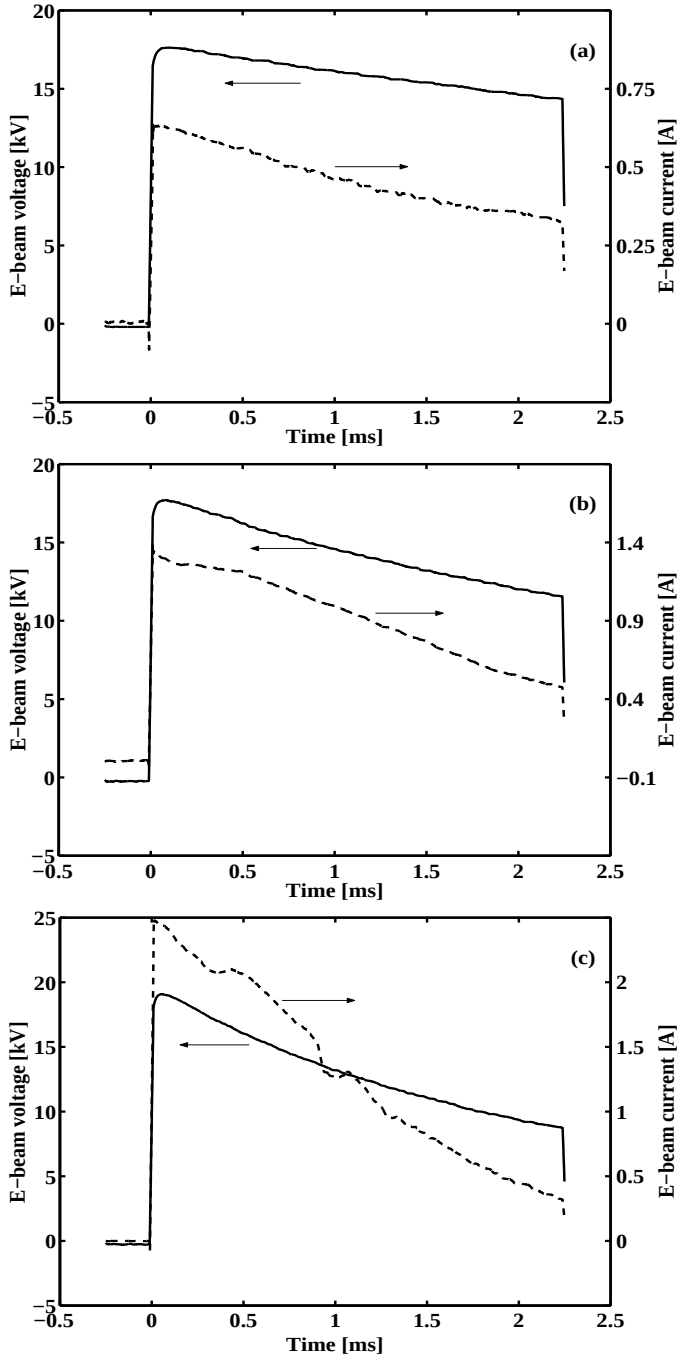

Figure 6.3: Raw measurements of the electron-beam voltage (solid line) and current (dashed line) vs. time when only cathode 2 was operated (a), cathodes 2 and 4 were operated (b), and all cathodes were operated (c).

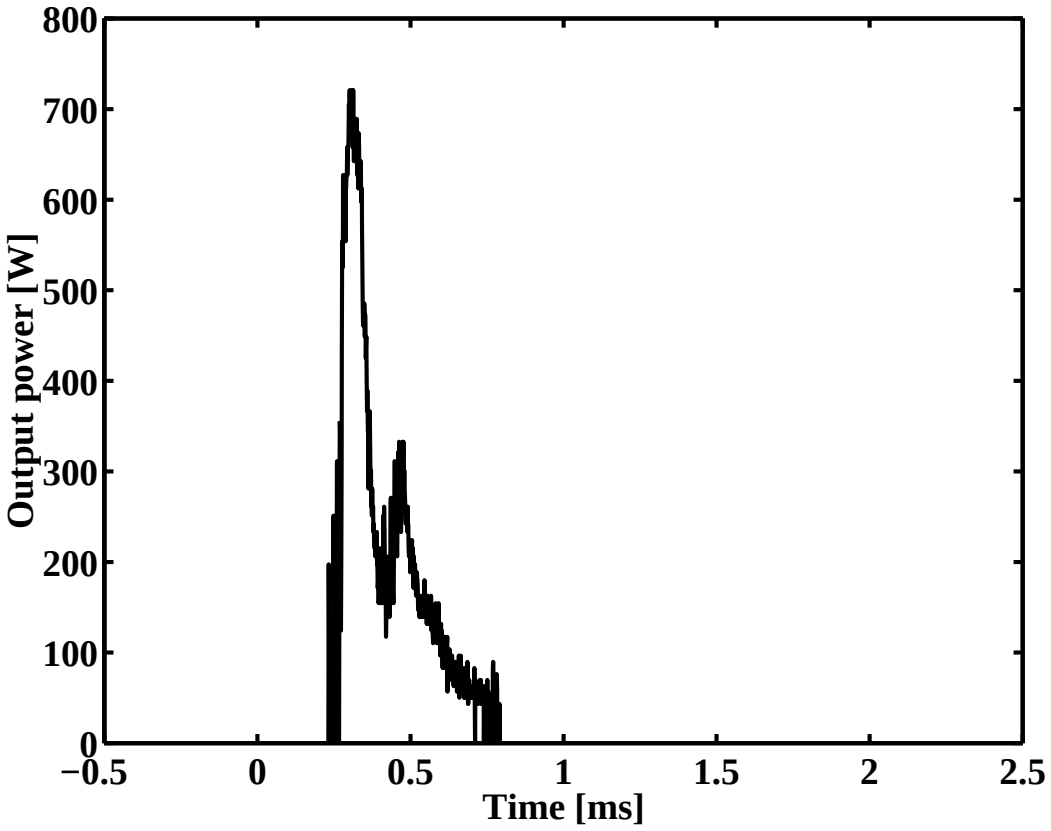

Figure 6.4: Raw measurement of the microwave output power when all cathodes were operated. The corresponding electron-beam voltage and current are shown in Fig. 6.3(c).

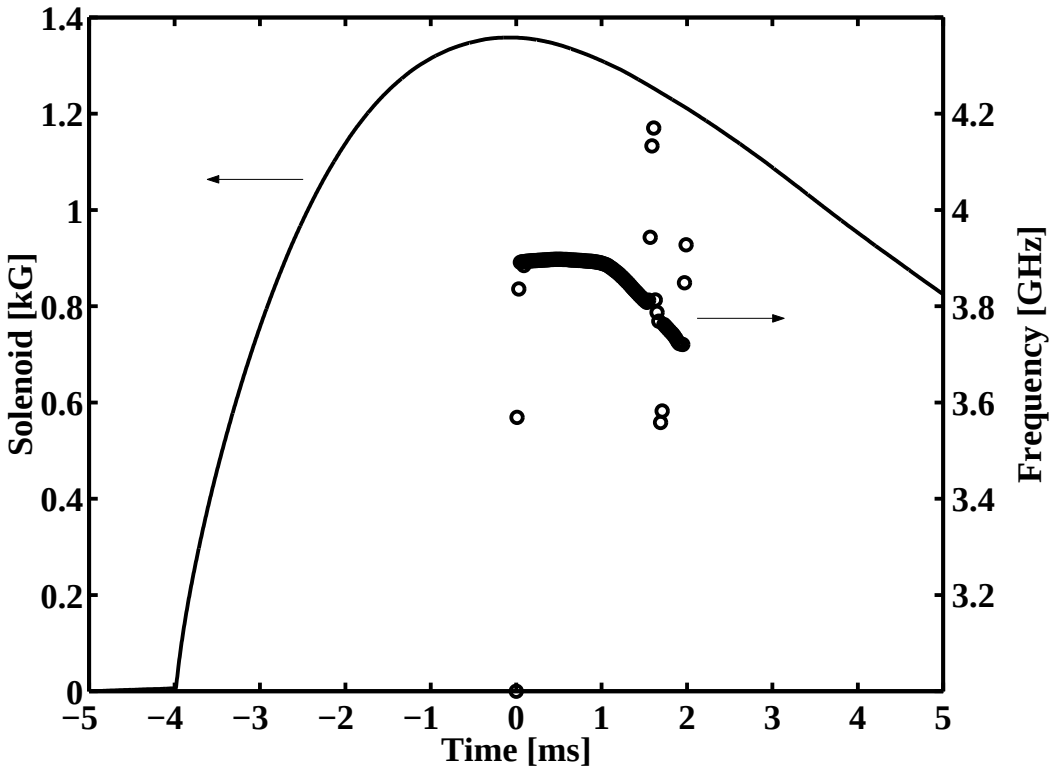

Figure 6.5: Raw measurements of the axial magnetic field (solid line) and frequency (circles) during an RF pulse.

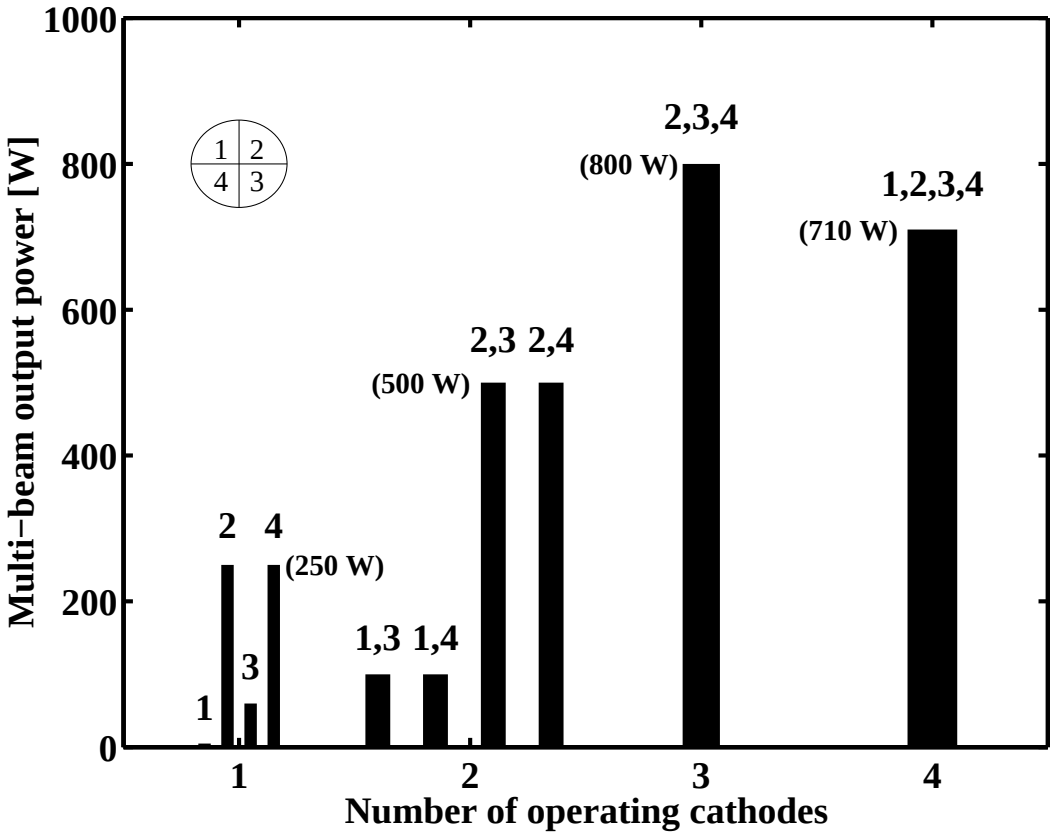

Figure 6.6: Summary of the multi-beam output power vs. the number of operating cathodes for the first configuration (no reflector inside the kicker pipe). The operating cathode numbers are indicated above the bars.

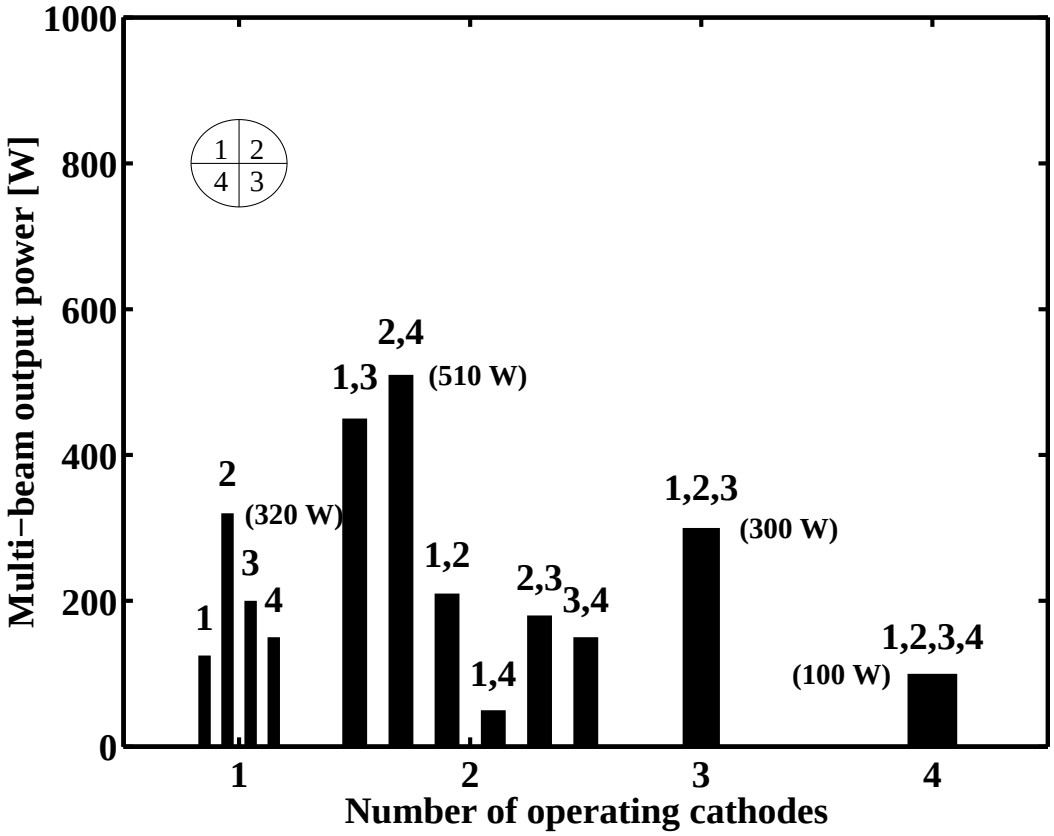

Figure 6.7: Summary of the multi-beam output power vs. the number of operating cathodes for the second configuration (with additional reflector inside the kicker pipe). The operating cathode numbers are indicated above the bars.

power was 710 W which corresponds to an interaction efficiency of 2.0%. The pulse duration seen (with respect to half-power) is $\sim$ 100 μs and the measured frequency during the pulse was 3.9 GHz.

Raw measurements of the axial magnetic field and frequency are shown in Fig. 6.5. It is seen that a frequency of 3.9 GHz and 1 ms long was measured when the magnetic field was between 1.30–1.35 kG. This frequency was obtained for all the RF measurements. As seen in Fig. 6.2, this frequency is within the pass-band of the periodic waveguide.

A summary of the multi-beam output power vs. the number of operating cathodes, for the first configuration, is presented in Fig. 6.6. Output powers of 3, 250, 60, or 250 W were measured from separate operation of cathodes 1, 2, 3, or 4, respectively. An output power of 100 W was measured when cathode 1 was operated together with 3 or 4, and 500 W for the combination of cathode 2 with 3 or 4. An output power of 800 W was measured for a combined operation of cathodes 2,3, and 4, and an output power of 710 W was measured for a full multi-beam operation. These results were collected out of tens of operating shots.

It is seen that the contribution of each of the second, third, or fourth electron-beam to the output power is $\sim 250\ W$, although the separate measurement of cathode 3 indicated only 60 W power. The operation of the first cathode with any of the others caused a reduction of the output power by

150 W for the two-beam operation cases and by 90 W for the four-beam case.

Due to the poor current of the first electron beam, and the output power decrease when this beam was operated, the device was opened for inspection. A mechanical movement of ~ 1 mm in the radial position of the electron-gun array towards the first cathode has been seen, and corrected. In addition, the two transverse reflector plates were added inside the kicker pipe, as described for the second configuration.

An equal collector current of 0.3 A at beam voltage of 13.5 kV was measured from separate operation of each electron-beam. The current transmission was 50% with respect to the input current. The collector current was increased proportionally with any combination of several electron-beams operated simultaneously.

A summary of the multi-beam output power vs. the number of operating cathodes, for the second configuration, is presented in Fig. 6.7. Output powers of 125, 510, 210, and 150 W were measured from separate operation of cathodes 1, 2, 3, and 4, respectively. Output powers of 450 or 510 W were measured for diagonal operation of cathodes 1,3 or 2,4, respectively. Operation of two adjacent cathods yielded output powers of 210, 50, 110, or 150 W, respectively. An output power of 300 W was measured for a combined operation of cathodes 1,2, and 3, and an output power of 100 W was measured for a full multi-beam operation. These results were collected

out of tens of operating shots.

It is seen that the contribution of each of the diagonal electron-beams to the output power is summed to $\sim 500\ W$, while the contribution of each of the adjacent electron-beams to the output power is subtracted to $\sim$ 100–200 W. The contribution of the first three electron-beams is in the order of a single electron beam, while the power of full multi-beam operation is less than the single cathode operation cases.

6.4 Discussion

A first operation of a four-beam CRM is demonstrated experimentally in this chapter. A maximum output power was obtained at 3.9 GHz, within the pass-band of the periodic waveguide. It is noted that the cutoff frequency of a hollow waveguide with the same diameter is 2.2 GHz. The axial magnetic field measured was 1.35 kG which corresponds to a cyclotron frequency of 3.67 GHz for a beam voltage of $\sim$ 15 kV. This result points out that the interaction occurred with a forward wave.

In the first configuration, a maximum output power of 800 W was obtained from a combined operation of beams 2,3, and 4. Although 60 W was measured in a separate operation of the third electron beam, a contribution of 250 W is attributed to each of these beams. The interaction efficiency of

2% is probably related to a wide beam velocity spread, which was larger than the designed value. Nevertheless, the positive balance to the output power from the simultaneous operation of these three beams might result from a possible synergistic effect.

The operation of the first electron-beam, which had the radial mechanical movement of $\sim$ 1 mm, resulted in a decrease of the output power. This result is important because an improper mechanical deviation might result in a deterioration instead of integration of the output power, as expected for the multi-beam operation.

In the second configuration, an output power summation of $\sim$ 500 W was obtained for only the two cases of two diagonal cathode operation. The other cases, when adjacent cathodes were operated together, resulted with a power subtraction. These results are probably related to the reflector inside the kicker region, which may reflected the *em* wave with a destructive interference.

The result obtained in the two configurations are important for designing coupled multi-beam CRMs. A special care is required in the cavity design and in its output coupling in order to enable the total power summation obtained in the first configuration. Separate electron beam tuning, such as varying the voltage of each beam, might also contribute for in-phase power summation, as in the uncoupled CRM-array. Voltage tuning might also compensate pos-

sible spatial variation in the axial magnetic field strength. A further care is probably needed in order to prevent transverse waves in a large multi-beam CRM array consisting of a wide cross section periodic waveguide [86].

The periodic waveguide enables a selective mode operation with a relatively wide cross-section, which can reduce the problem of mode competition. Furthermore, it provides an artificial loading which slows the wave, and can enable a low-voltage operation design. However, a careful cavity and coupling design must be considered.

Multi-electron beam schemes might be important for high-power gyrotrons, in which many low-voltage low-current electron beams may replace the single high-power beam in the conventional devices. Such approach might lead to a design of tens of multi-beam channels, each consisting of low beam voltage and current of several kilovolt and few Ampere, respectively, to yield a total power of ~ 1 MW [87].

Chapter 7

Discussion

This thesis presents features of CRM-arrays, as well as scientific results applicable for other studies. Both uncoupled and coupled CRM-arrays were studied at low electron beam voltages and currents (< 20 kV, < 1 A), and were aimed for compactness in their overall size.

The uncoupled CRM-array concept described in Chapter 2 demonstrates a novel type of an active antenna array for high-power microwaves. The CRM-elements combine their total high-power microwave radiation in the far field. The power and directivity are increased as the number of operating elements is increased. An analog electronic control of the electron beams allows a wide radiation steering range (up to $\pm 35°$). The CRM-array is characterized by its elements. The results of the three possible types of related elements are discussed below.

The distributed-loss CRM amplifier experiment described in Chapter 3 demonstrates the gain and phase control abilities expected from the CRM-element. A maximum gain of 26 dB with output power of 0.63 kV and 12% efficiency is obtained at 7.3 GHz. A full 360° phase-delay range with a constant gain of 23 dB is achieved by tuning the magnetic field and compensating with the electron-beam current.

Pulse and frequency modulations are presented by the feedback-controlled CRM-oscillator experiment in Chapter 4. A 0.2 MHz pulse modulation rate is obtained by the feedback switching. The frequency modulation is obtained by varying the feedback phase-shift, where the 8.8 MHz maximum frequency modulation depth obtained is determined by the round-trip time. A drift in the axial magnetic field due to the pulsed operation of the solenoid caused a shift in the excited frequencies. The phase-shift due to the magnetic field drift is in agreement with the results presented in Chapter 3. A frequency ambiguity is disabled if the maximum modulation depth is more than the CRM instantaneous band-width.

The feedback-controlled concept could be incorporated in CRM-array oscillators, where the sampling of one CRM-element output can be controlled to modulate in-phase the entire array. The simplicity of this method is attractive because the modulation is carried at the low CRM-amplifier input power, and does not require an external local oscillator.

Chapter 5 present a new tunability feature by incorporating a ferrite material to guide the *em* wave of the CRM. A 13% tuning range around 9 GHz is calculated for a low beam voltage of 7.5 kV and slow-wave interaction in the Weibel regime. Such tuning range in a low-voltage operation could not be achieved in unloaded CRMs. This study might lead to development of tunable CRM-arrays. The ferrite-loading may also be tapered in order to compensate possible spatial variations of the magnetic field in wide cross-sectioned CRM-arrays.

A first demonstration of a four-beam CRM is presented experimentally in Chapter 6. A 0.8 kW output power is obtained by the simultaneous operation of three electron beams, where the output power obtained for a separate operation of each beam is 250 W or less. Thus, a possible synergism effect is considered. The operation of the additional electron-beam, which had some slight mechanical offset, caused an internal absorption and resulted in a power decrease to 710 W.

A second configuration was operated, in which the mechanical offset was fixed and a reflector was added in the beginning of the interaction region. The output power from the simultaneous operation of two diagonal channels resulted in a power summation to ~ 500 W, while the operation of adjacent channels resulted in a decrease of the output power. However, the device was not operated with the expected improved configuration, of the accurate

mechanical position and without the additional reflector.

The CRM-array concept may lead to a compact low-voltage device with a relatively small system overhead, and it may alleviate problems of output windows and mode-coupling effects, which characterize high power gyrotrons. The CRM-array antenna could be used in various applications, including radars, power beaming, plasma heating, and material processing.

A further study towards practical implementations of phased-controlled CRM-amplifier elements based on the distributed-loss concept [10, 42] should include: a sensitivity analysis of the gain and phase-delay controllability with respect to all CRM operating parameters, including also beam voltage, electron spread, and interaction length, and a phase-jitter and stability analysis. Improved schemes should also consider decreasing the noise figure in order to suit the needs in radar and communication applications.

It is noted that the tendency to operate at frequencies higher than several giga-hertz might encounter problems related to keeping a dense array in which the distance between its elements is no more than half a wavelength. In particular, due to the space required for the electron-guns, flanges, and the waveguide wall-thickness with respect to its aperture.

The performance and cost of the internal phase-control should be compared to the alternate use of common phase-shifters located before their inputs. However, this study is also significant for other applications in

which phase-stability is important, such as driving electron guns for colliders [38, 39].

Controlled-feedback CRM oscillators could be used in high-power radar application for pulse, stepped-frequency, or linear-frequency modulation. Further theoretical studies are needed (a) to determine the excited frequencies, the quality, bandwidth, and the efficiency of such device, (b) to obtain limitations for maximum available bandwidth without a frequency ambiguity, (c) to determine the maximum modulation rate with respect to the system parameters, and (d) to analyze locking methods that incorporate the controlled-feedback scheme as described in Ref. [58] for FELs. Further experimental studies may include characterization of the feedback-controlled operation such as stability, coherence, and driving power, as well as measurements of some of the theoretical goals described above.

Further theoretical and experimental studies are needed in order to evaluate the features of the ferrite-guided CRM's and to examine their characteristics. These include non-linear analysis in a wide range of parameters, taking into account multi-mode transverse effects, ferrite losses, and velocity spread. Experimental tools should be developed in order to easily find a match of the tunable waveguide to the corresponding tunable cyclotron frequency. An experimental demonstration of the ferrite-loaded CRM concept is considered [88].

The CRM-element can determine the characteristics of the CRM-array. For the active CRM-array antennas, future studies should include an analysis of the coupling between the CRM-elements, and the influence of active reflections on the array performance. The influence of active reflections could be alleviated in distributed-loss schemes due to their high (backward) insertion-loss. An experimental study of an active CRM-array antenna is also desired.

Further research towards the realization of high-power multi-beam CRMs might include analysis of wide cross-sectioned periodic structures. Such structures may support a high filling-factor for the multi-beam interaction along with a good mode-selectivity. Internal reflections and output coupling should also be taken into account.

It is important to determine conditions in which the multi-beam CRM-array is preferred over the conventional single-beam device. In particular, a study towards possible synergism effect and to evaluate the possible interaction efficiency. Due to the off-axis locations of the electron beams, it will be important to obtain a proper electron-optics design and a proper depressed collector. A separate tuning of each beam voltage is of interest, in order to create the optimal conditions for the integrated power. These aspects involve, however, a further technological complexity.

The research of cold-cathode electron-beam sources is important for multi-beam devices. Such cathodes can alleviate the need for a good vacuum con-

dition and also decrease significantly the device cost. Ferroelectric based electron-guns are good candidates for this purpose [89, 90].

In our vision, future CRM-arrays might consist of a multi-beam electron gun capable of a total high-current. The low-voltage operation will result in a decrease in the system overhead. The low-current operation of each beam will result in a lower space-charge and a higher beam quality. A kicker array might consist of constant magnets located near their corresponding beams. Improved mode-selectivity, tunability, and filling factor would be obtained by a periodic structure consisting also ferrite loading. The total high power would be radiated through a wide aperture to alleviate the window heating problem, and radiation-beam steering in space will be achieved by controlling the electron-beam parameters [19].

Bibliography

[1] A. V. Gaponov-Grekhov and V. L. Granatstein, *Applications of High-Power Microwaves*. Norwood MA: Artech House, 1994. and references therein.

[2] G. S. Nusinovich and E. Jerby, Eds., *IEEE Transactions on Plasma Science*. vol. 27, 2, 1999.

[3] V. A. Flyagin, A. V. Gaponov, M. I. Petelin, and V. Yulpatov, "The gyrotron," *IEEE Trans. Microwave Theory Tech.*, vol. MTT-25, pp. 514–521, 1977.

[4] V. L. Granatstein, *Gyrotron experimental studies*. Norwood, MA: Artech House, 1987.

[5] G. Link, L. Feher, M. Thumm, H-J. Ritzhaupt-Kleissl, R. Bohme, and A. Weisenburger, "Sintering of advanced ceramics using a 30-ghz, 10-kw,

cw industrial gyrotron," *IEEE Transactions on Plasma Science*, vol. 27, pp. 547–554, 1999.

[6] V. Erckmann, W. Kasparek, G. A. Muller, P. Schuller, and M. Thumm, "Electron cyclotron resonance heating transmission line and launching system for the wendelstein vii-as stellarator," *Fusion Technology*, vol. 17, pp. 76–85, 1990.

[7] Q. S. Wang, D. B. McDermott, A. T. Lin, N. C. Jr. Luhmann, and K. R. Chu, "High power carm for high gradient rf linac," in *IEEE International Conference on Plasma Science*, pp. 194–195, New York, NY, 1990.

[8] W. M. Manheimer, "On the possibility of high power gyrotrons for super range resolution radar and atmospheric sensing," *International Journal of Electronics*, vol. 72, pp. 1165–1189, 1992.

[9] For a recent update see M. Thumm, "State-of-the-art of high power gyro-devices and free electron masers update 2001," in *FZKA 6708*, Forschungszentrum Karlsruhe, Technik und Umwelt, Wissenschaftliche Berichte, February 2002.

[10] K. R. Chu, H. Y. Chen, C. L. Hung, T. H. Chang, L. R. Barnett, S. H. Chen, T. T. Yang, and D. J. Dialetis, "Theory and experiment of

ultrahigh-gain gyrotron traveling wave amplifier," *IEEE Transactions on Plasma Science*, vol. 27, pp. 391–404, 1999.

[11] T. Idehara, I. Ogawa, S. Mitsudo, M. Pereyaslavets, N. Nishida, and K. Yoshida, "Development of frequency tunable, medium power gyrotrons (gyrotron fu series) as submillimeter wave radiation sources," *IEEE Transactions on Plasma Science*, vol. 27, pp. 340–354, 1999.

[12] V. Erckmann, G. Dammertz, D. Dorst, L. Empacher, W. Forster, G. Gantenbein, T. Geist, W. Kasparek, H. P. Laqua, G. A. Muller, M. Thumm, M. Weissgerber, and H. Wobig, "Ecrh and eccd with high power gyrotrons at the stellarators w7-as and w7-x," *IEEE Transactions on Plasma Science*, vol. 27, pp. 538–534, 1999.

[13] J. Teniente, R. Gonzalo, C. del Rio, J. Marti-Canales, M. Sorolla, A. Fernandez, K. M. Likin, and R. Martin, "Corrugated horn antenna for low-power testing of the quasioptical transmission lines at tj-ii stellerator," *International Journal of Infrared and Millimeter Waves*, vol. 20, pp. 1757–1767, 1999.

[14] V. L. Bratman, N. S. Ginzburg, G. S. Nusinovich, M. I. Petelin, and P. Strelkov, "Relativistic gyrotrons and cyclotron autoresonance masers," *International Journal of Electronics*, vol. 51, pp. 541–567, 1981.

[15] S. H. Gold and G. S. Nusinovich, "Review of high-power microwave source research," *Review of Scientific Instruments*, vol. 68, pp. 3945–3974, 1997.

[16] C. Liu and T. M. Antonsen, Jr., "Implication of dc-space-charge-induced velocity spread on gyrotron gun performance," *IEEE Transactions on Plasma Science*, vol. 26, pp. 825–834, 1998.

[17] A. Kasugai, K. Sakamoto, K. Takahashi, M. Tsuneoka, T. Kariya, T. Imai, O. Braz, M. Thumm, J. R. Brandon, R. S. Sussman, and A. Beale, "Cvd diamond window for high-power and long pulse millimeter wave transmission," *Review of Scientific Instruments*, vol. 69, pp. 2160–2165, 1998.

[18] E. Jerby, M. Korol, L. Lei, V. Dikhtiar, R. Milo, and I. Mastovsky, "Cyclotron-resonance maser arrays - concept, theory, and experiments," in *Digest of the 22 Int'l Conf. Infrared and Millimeter Waves*, pp. 65–66, Wintergreen, Virginia, July 20-25 1997.

[19] E. Jerby, A. Kesar, M. Korol, L. Lei, and V. Dikhtiar, "Cyclotron-resonance maser arrays," *IEEE Transactions on Plasma Science*, vol. 27, pp. 445–455, 1999. and references therein.

[20] A. Kesar and E. Jerby, "Radiation beam steering by cyclotron-resonance maser array," *Physical Review E*, vol. 59, pp. 2464–2466, 1999.

[21] A. Kesar and E. Jerby, "Phase and gain measurements in a distributed-loss cyclotron-resonance maser amplifier," *Physical Review E*, vol. 65, pp. 036503/1–6, 2002.

[22] A. Kesar, D. Blank, and E. Jerby, "Amplitude locking in a gyro-TWT amplifier with a delayed feedback," in *IEEE Int'l Conference on Plasma Science*, p. 188, Banff, Alberta, Canada, May 26-30 2002.

[23] A. Kesar, D. Blank, and E. Jerby, "Cyclotron-resonance maser array antenna," in *IEEE Int'l Conference on Plasma Science*, p. 150, Banff, Alberta, Canada, May 26-30 2002.

[24] M. Korol and E. Jerby, "Linear analysis of a multibeam cyclotron-resonance maser array," *Physical Review E*, vol. 55, pp. 5934–5947, 1997.

[25] L. Lei and E. Jerby, "Cyclotron maser experiment in two-dimensional array," *SPIE Proc.*, vol. 2843, pp. 30–37, 1996. Also submitted to Physical Review E.

[26] G. S. Nusinovich, B. Levush, and B. G. Danly, "Theory of multi-beam stagger-tuned gyroklystron," in *Digest of the 22 Int'l Conf. Infrared and Millimeter Waves*, pp. 243–244, Wintergreen, Virginia, July 20-25 1997.

[27] A. V. Gaponov-Grekhov and V. L. Granatstein, *Applications of high-power microwaves*. Boston: Artech House, 1994.

[28] J. Benford and J. Swegle, *High-power microwaves*. Boston: Artech House, 1992.

[29] Y. Pinhasi, I. M. Yakover, A. L. Eichenbaum, and A. Gover, "Efficient electrostatic-accelerator free-electron masers for atmospheric power beaming," *IEEE Transactions on Plasma Science*, vol. 24, pp. 1050–1057, 1996.

[30] D. C. Jenn, "RPVs. Tiny, microwave powered, remotely piloted vehicles," *IEEE Potentials*, vol. 16, pp. 20–22, 1997.

[31] R. E. Collin, *Antennas and radiowave propagation*. New York: McGraw-Hill, 1985.

[32] S. Fukao, T. Sato, T. Tsuda, S. Kato, K. Wakasugi, and T. Makihira, "The mu radar with an active phased array system 1. antenna and power amplifiers," *Radio Science*, vol. 20, pp. 1155–1168, 1985.

[33] S. H. Colodny and R. L. Crane, "Active-array antenna beam shaping for direct broadcast satellite and other applications," *RCA Review*, vol. 46, pp. 376–392, 1985.

[34] E. Jerby, "Angular steering of the free-electron-laser far-field-radiation beam," *Physical Review A*, vol. 41, pp. 3804–3811, 1990.

[35] A. Kesar and E. Jerby, "Power-beam steering by a CRM array," in *Int'l Research Workshop on CRMs and Gyrotrons*, p. 48, Kibbutz Ma'ale Hachamisha, Israel, May 18-21 1998.

[36] E. Jerby, "Linear analysis of periodic-waveguide cyclotron maser interaction," *Physical Review E*, vol. 49, pp. 4487–4496, 1994.

[37] M. Cecere and T. C. Marshall, "A free electron laser experiment on 'angular steering'," *IEEE Transactions on Plasma Science*, vol. 22, pp. 654–658, 1994.

[38] V. L. Granatstein and W. Lawson, "Gyro-amplifiers as candidate rf drivers for tev linear colliders," *IEEE Transactions on Plasma Science*, vol. 24, pp. 648–665, 1996.

[39] W. Lawson, M. Castle, S. Gouveia, V. L. Granatstein, B. Hogan, G. Nusinovich, M. Reiser, and I. Spassovsky, "Progress in the development of relativistic gyroamplifiers for future linear colliders," in *25th International Conference on Infrared and Millimeter Waves*, pp. 107–108, IEEE, Piscataway, NJ, S. Liu and X. Shen ed., Sept. 12-15 2000.

[40] Q. S. Wang, D. B. McDermott, and N. C. Luhmann, Jr., "Operation of a stable 200-kw second-harmonic gyro-twt amplifier," *IEEE Transactions on Plasma Science*, vol. 24, pp. 700–706, 1996.

[41] G. S. Nusinovich, J. Rodgers, W. Chen, and V. L. Granatstein, "Phase stability in gyro-traveling-wave-tubes," *IEEE Transactions on Electron Devices*, vol. 48, pp. 1460–1468, 2001.

[42] K. R. Chu, L. R. Barnett, H. Y. Chen, S. H. Chen, Ch. Wang, Y. S. Yeh, Y. C. Tsai, T. T. Yang, and T. Y. Dawn, "Stabilization of absolute instabilities in the gyrotron traveling wave amplifier," *Physical Review Letters*, vol. 74, pp. 1103–1106, 1995.

[43] V. L. Bratman and S. V. Samsonov, Private communication.

[44] W. B. Herrmannsfeldt, *Egun - an electron optics and gun design program.* Stanford, California: Stanford Linear Accelerator Center, Stanford University, October 1988.

[45] K. R. Chu, Private communication.

[46] G. S. Nusinovich and M. Walter, "Theory of the inverted gyrotwystron," *Physics of Plasmas*, vol. 4, pp. 3394–3402, 1997.

[47] K. T. Nguyen, J. P. Calame, D. E. Pershing, B. G. Danly, M. Garven, B. Levush, and T. M. Antonsen, Jr., "Design of a ka-band gyro-twt for

radar applications," *IEEE Transactions on Electron Devices*, vol. 48, pp. 108–115, 2001.

[48] P. E. Ferguson, G. Valier, and R. S. Symons, "Gyrotron-twt operating characteristics," *IEEE Transactions on Microwave Theory and Techniques*, vol. 29, pp. 794–799, 1981.

[49] T. Kikunaga, H. Asano, Y. Yasojima, F. Sato, and T. Tsukamoto, "A 28 ghz gyrotron with a permanent magnet system," *International Journal of Electronics*, vol. 79, pp. 655–663, 1995.

[50] D. B. McDermott, A. J. Balkcum, and N. C. Luhmann, Jr., "35-ghz 25-kw cw low-voltage third-harmonic gyrotron," *IEEE Transactions on Plasma Science*, vol. 24, pp. 613–619, 1996.

[51] K. Koppenburg, G. Dammertz, M. Kuntze, B. Piosczyk, and M. Thumm, "Fast frequency-step-tunable high-power gyrotron with hybrid-magnet-system," *IEEE Transactions on Electron Devices*, vol. 48, pp. 101–107, 2001.

[52] A. H. McCurdy, "Nonlinear theory of large-signal mode locking in a gyrotron oscillator," *Applied Physics Letters*, vol. 66, pp. 1845–1847, 1995.

[53] Hao Wu, RongLin Liou, and A. H. McCurdy, "Pic code simulation of pulsed radiation in a tapered closed-cavity gyrotron," *IEEE Transactions on Plasma Science*, vol. 24, pp. 606–612, 1996.

[54] A. H. McCurdy, C. M. Armstrong, W. M. Bollen, R. K. Parker, and V. L. Granatstein, "Improved oscillator phase locking by use of a modulated electron beam in a gyrotron," *Physical Review Letters*, vol. 57, pp. 2379–2382, 1986.

[55] C. S. Kou, S. H. Chen, L. R. Barnett, H. Y. Chen, and K. R. Chu, "Experimental study of an injection-locked gyrotron backward-wave oscillator," *Physical Review Letters*, vol. 70, pp. 924–927, 1993.

[56] E. Jerby, G. Bekefi, and J. S. Wurtele, "Observations of periodic intensity bursts during the start-up phase of a free-electron-laser oscillator," *Physical Review Letters*, vol. 66, pp. 2068–2071, 1991.

[57] E. Jerby, G. Bekefi, and J. S. Wurtele, "Experimental and theoretical study of periodic intensity bursts in the start-up phase of a free-electron laser oscillator," *IEEE Journal of Quantum Electronics*, vol. 27, pp. 2512–2521, 1991.

[58] E. Jerby and G. Bekefi, "Am mode-locking of a free-electron laser oscillator," *IEEE Journal of Quantum Electronics*, vol. 29, pp. 2845–2851,

1993.

[59] D. Blank, Private communication.

[60] K. R. Chu and J. L. Hirshfield, "Comparative study of the axial and azimuthal bunching mechanisms in electromagnetic cyclotron instabilities," *Phys. Fluids*, vol. 21, pp. 461–466, 1978.

[61] T. Idehara, T. Tatsukawa, S. Matsumoto, K. Kunieda, K. Hemmi, and T. Kanemaki, "Development of high-frequency cyclotron harmonic gyrotron oscillator," *Phys. Lett. A*, vol. 132, pp. 344–346, 1988.

[62] H. Guo, L. Chen, H. Keren, J. L. Hirshfield, S. Y. Park, and K. R. Chu., "Measurements of gain for slow cyclotron waves on an annular electron beam," *Phys. Rev. Lett.*, vol. 49, pp. 730–733, 1982.

[63] M. Einat and E. Jerby, "Normal and anomalous doppler effects in a dielectric loaded cyclotron-resonance maser oscillator," *Phys. Rev. E.*, vol. 56, p. 5996, 1997.

[64] E. Jerby and G. Bekefi, "Cyclotron maser experiments in a periodic-waveguide," *Physical Review E*, vol. 48, pp. 4637–4641, 1993.

[65] E. Jerby, A. Shahadi, V. Grinberg, V. Dichtiar, E. Agmon, H. Golombek, V. Trebich, M. Bensal, and G. Bekefi, "Cyclotron maser oscillator exper-

iments in a periodically loaded waveguide," *IEEE J. Quantum Electron*, vol. 31, pp. 970–979, 1995.

[66] B. I. Ivanov, D. V. Gorozhanin, and V. A. Miroshnichenko, "Observation of amplification by the anomalous doppler effect," *Pis'ma Zh. Tekh. Fiz.*, vol. 5, pp. 1112–1116, 1979. Sov. Tech. Phys. Lett., Vol. 5, pp. 464-465, 1979.

[67] A. N. Didenko, A. R. Borisov, G. P. Fomenko, A. S. Shlapakovskii, and YuG. Shtein, "Cyclotron maser using the anomalous doppler effect," *Pis'ma Zh. Tekh. Fiz.*, vol. 9, pp. 1331–1334, 1983. [Translated from Sov. Tech. Phys. Lett., Vol. 9, pp. 572-573, 1983].

[68] E. Jerby, Unpublished.

[69] A. W. Trivelpiece, A. Ignatius, and P. C. Holscher, "Backward waves in longitudinally magnetized ferrite rods," *J. Appl. Phys.*, vol. 32, p. 259, 1961.

[70] J. Spector and A. W. Trivelpiece, "Slow waves in ferrites and their interaction with electron streams," *J. Appl. Phys.*, vol. 35, no. 7, pp. 2030–2039, 1964.

[71] R. Chatterjee, *Advanced Microwave Engineering Special Advanced Topics*. Chichester: Ellis Horwood Publishers, 1988.

[72] R. E. Collin, *Foundations for Microwave Engineering.* New York: McGraw Hill, 1992.

[73] E. Jerby, A. Kesar, A. Aharony, and G. Breitmeier, "Ferrite-guided cyclotron-resonance maser," *Physical Review E*, vol. 65, pp. 066502/1–8, 2002.

[74] A. J. Baden Fuller, "Microwave propagation through round waveguide partially filled with ferrite," *Proc. Instn. Elect. Engnrs.*, vol. 108C, pp. 339–348, 1961.

[75] G. F. Brand, T. Idehara, T. Tatsukawa, and I. Ogawa, "Mode competition in a high harmonic gyrotron," *International Journal of Electronics*, vol. 72, pp. 745–758, 1992.

[76] G. P. Saraph, T. M. Antonsen, Jr., G. S. Nusinovich, and B. Levush, "Nonlinear theory of stable, efficient operation of a gyrotron at cyclotron harmonics," *Physics of Fluids B*, vol. 5, pp. 4479–4485, 1993.

[77] G. Gantenbein, E. Borie, O. Dumbrajs, and M. Thumm, "Design of a high order volume mode cavity for a 1 mw/140 ghz gyrotron," *International Journal of Electronics*, vol. 78, pp. 771–787, 1995.

[78] W. H. Kummer, "Broad-band microwave electronically scanned direction finder," *IEEE Transactions on Antennas and Propagation*, vol. AP-31, pp. 18–26, 1983.

[79] J. R. Sirigiri, K. E. Kreischer, J. Machuzak, I. Mastovsky, M. A. Shapiro, and R. J. Temkin, "Photonic-band-gap resonator gyrotron," *Physical Review Letters*, vol. 86, pp. 5628–5631, 2001.

[80] R. B. Palmer, R. C. Fernow, J. Fischer, J. C. Gallardo, H. G. Kirk, S. Ulc, H. Wang, Y. Zhao, K. Eppley, W. Herrmannsfeldt, R. Miller, and D. Yu, "The cluster klystron demonstration experiment," *Nuclear Instruments and Methods in Physics Research Section A*, vol. 366, pp. 1–16, 1995.

[81] G. Bekefi, "Double-stream cyclotron maser," *Journal of Applied Physics*, vol. 71, pp. 4128–4131, 1992.

[82] G. S. Nusinovich, B. Levush, and B. Danly, "Theory of multi-beam stagger-tuned gyroklystrons," *IEEE Transactions on Plasma Science*, vol. 26, pp. 475–481, 1998.

[83] L. Lei and E. Jerby, "Two-dimensional cyclotron-resonance maser array: Spectral measurements with one and two electron beams," *Physical Review E*, vol. 59, pp. 2322–2329, 1999.

[84] L. Lei, *Multibeam cyclotron-resonance maser array.* PhD thesis, Faculty of Engineering, Tel-Aviv University, 2002.

[85] A. Kesar, Internal report, 2002.

[86] M. A. Shapiro, Private communication.

[87] E. Jerby, Seminar on cyclotron-resonance masers, Dept. of Physical Electronics, Faculty of Engineering, Tel Aviv University, March 2001.

[88] E. Jerby *et al.*, In preparation.

[89] M. Einat, E. Jerby, and G. Rosenman, "High-repetition-rate ferroelectric-cathode gyrotron," *Applied Physics Letters*, vol. 79, pp. 4097–4099, 2001.

[90] M. Einat, E. Jerby, and G. Rosenman, "Spectral measurements of gyrotron oscillator with ferroelectric electron gun," *Applied Physics Letters*, vol. 81, pp. 1347–1349, 2002.